Title

FULLY COUPLED SIMULATION OF COSMIC REIONIZATION. II. RECOMBINATIONS, CLUMPING FACTORS, AND THE PHOTON BUDGET FOR REIONIZATION

Journal

The Astrophysical Journal, 789(2)

ISSN

0004-637X 1538-4357

Authors

So, Geoffrey C
Norman, Michael L
Reynolds, Daniel R
et al.

Publication Date

2014-07-10

DOI

10.1088/0004-637X/789/2/149

Peer reviewed

The Astrophysical Journal, 789:149 (29pp), 2014 July 10 doi:10.1088/0004-637X/789/2/149

FULLY COUPLED SIMULATION OF COSMIC REIONIZATION. II. RECOMBINATIONS, CLUMPING FACTORS, AND THE PHOTON BUDGET FOR REIONIZATION

Geoffrey C. So (蘇治平)[1], Michael L. Norman[1,2], Daniel R. Reynolds[3], and John H. Wise[4]
[1] CASS, University of California, San Diego, 9500 Gilman Drive, La Jolla, CA 92093-0424, USA
[2] SDSC, University of California, San Diego, 9500 Gilman Drive, La Jolla, CA 92093-0505, USA
[3] Southern Methodist University, 6425 Boaz Lane, Dallas, TX 75205, USA
[4] Center for Relativistic Astrophysics, Georgia Institute of Technology, 837 State Street, Atlanta, GA 30332, USA
Received 2013 November 7; accepted 2014 May 10; published 2014 June 24

ABSTRACT

We use a fully coupled cosmological simulation including dark matter dynamics, multispecies hydrodynamics, nonequilibrium chemical ionization, flux-limited diffusion radiation transport, and a parameterized model of star formation and feedback (thermal and radiative) to investigate the epoch of hydrogen reionization in detail. In this paper, the first of several application papers, we investigate the mechanics of reionization from stellar sources forming in high-z galaxies, the utility of various formulations for the gas clumping factor on accurately estimating the effective recombination time in the intergalactic medium (IGM), and the photon budget required to achieve reionization. We also test the accuracy of the static and time-dependent models of Madau et al. as predictors of reionization completion/maintenance. We simulate a *WMAP7* ΛCDM cosmological model in a 20 comoving Mpc cube, resolved with 800^3 uniform fluid cells and dark matter particles. By tuning our star formation recipe to approximately match the observed high-redshift star formation rate density and galaxy luminosity function, we have created a fully coupled radiation hydrodynamical realization of hydrogen reionization, which begins to ionize at $z \approx 10$ and is completed at $z \approx 5.8$ without further tuning. We find that roughly two ionizing photons per H atom are required to convert the neutral IGM to a highly ionized state. After reionization concludes, we find that the quantity $\dot{n}_{\rm ion} \times (1\ {\rm Gyr})/n_{\rm H}$ is ∼9 at $z = 5$, in rough agreement with measurements of the ionizing emissivity by Becker & Bolton. The complicated events during reionization that lead to this number can be generally described as inside-out, but in reality, the narrative depends on the level of ionization of the gas one attributes as being ionized. We find that the formula for the ionizing photon production rate needed to maintain the IGM in an ionized state derived by Madau et al. should not be used to predict the epoch of reionization completion because it ignores history-dependent terms in the global ionization balance which are not ignorable. We find that the time-dependent model for the ionized volume fraction $Q_{\rm H\,II}$ is more predictive, but overestimates the redshift of reionization completion $z_{\rm reion}$ by $\Delta z \approx 1$. We propose a revised formulation of the time-dependent model that agrees with our simulation to a few percent accuracy. Finally, we use our simulation data to measure the absorption of ionizing radiation due to circumgalactic gas resolved on our mesh and find $\bar{f}_{\rm esc}({\rm CGM}) \approx 0.7$.

Key words: cosmology: theory – intergalactic medium – large-scale structure of universe

Online-only material: color figures

1. INTRODUCTION

The Epoch of Reionization (EoR) is an active area of observational, theoretical, and computational research. Observations constrain the tail end of hydrogen reionization to the redshift range $z = 6$–8 (see reviews by Fan et al. 2006; Robertson et al. 2010). These observations include the presence of Gunn–Peterson troughs in the Lyα absorption spectra of high-redshift quasars (Songaila 2004; Fan et al. 2006), and the evolution of Lyα emitter luminosity function (Stark et al. 2010; Schenker et al. 2014). Observations from the *Wilkinson Microwave Anisotropy Probe* (*WMAP*) and *Planck* satellites tell us that the universe was substantially ionized by $z = 10$, but can say little about the reionization history or topology (Spergel et al. 2003; Komatsu et al. 2009; Jarosik et al. 2011; Planck Collaboration et al. 2013). High-redshift 21 cm observations hold forth great promise of elucidating the details of this transition (Barkana & Loeb 2007; Pritchard & Loeb 2012), but the results of these observations are still unknown.

It is believed that early star-forming galaxies provided the bulk of the UV photons responsible for reionization (Ouchi et al. 2010; Robertson et al. 2010, 2013; Ellis et al. 2013; Schenker et al. 2013), but early QSOs may have also contributed (Madau et al. 1999; Bolton & Haehnelt 2007; Haardt & Madau 2012). The "galaxy reionizer" hypothesis has been greatly strengthened by the recent advances in the study of high-redshift galaxies afforded by the IR-sensitive Wide Field Camera 3 on board the *Hubble Space Telescope* (e.g., Robertson et al. 2010, 2013; Bouwens et al. 2011a, 2011b; Schenker et al. 2012, 2013, 2014; Oesch et al. 2014; Schmidt et al. 2014). Within uncertainties, the luminosity function of $z = 6$ Lyman break galaxies appears to be sufficient to account for reionization at that redshift from a photon counting argument (Bolton & Haehnelt 2007; Robertson et al. 2010; Bouwens et al. 2012), but insufficient at $z = 8$ (Schmidt et al. 2014). Among the observational uncertainties are the faint-end slope of the galaxy luminosity function (Wise & Cen 2009; Labbé et al. 2010; Bouwens et al. 2012), the spectral energy distribution (SED) of the stellar population (Cowie et al. 2009; Willott et al. 2010; Haardt & Madau 2012), and the escape fraction of ionizing photons (Wyithe et al. 2010; Yajima et al. 2011; Mitra et al. 2013). Among the theoretical uncertainties are the number of ionizing photons per H atom required to bring the neutral intergalactic medium (IGM) to its highly ionized state by $z = 6$, the clumping factor correction to the mean IGM recombination time (Pawlik et al. 2009; Raicevic & Theuns 2011; Finlator et al. 2012; Shull et al. 2012; Robertson et al.

2013), and the contribution of Pop III stars and accreting black holes to the early and late stages of reionization (Bolton & Haehnelt 2007; Trac & Gnedin 2011; Ahn et al. 2012).

When assessing whether an observed population of high-z galaxies is capable of reionizing the universe (e.g., Robertson et al. 2013), observers often use the criterion derived by Madau et al. (1999) for the ionizing photon volume density $\dot{\mathcal{N}}_{\rm ion}$ necessary to maintain the clumpy IGM in an ionized state:

$$\dot{\mathcal{N}}_{\rm ion}(z) = \frac{\bar{n}_{\rm H}(0)}{\bar{t}_{\rm rec}(z)} = (10^{51.2}\ {\rm s}^{-1}\ {\rm Mpc}^{-3}) \left(\frac{C}{30}\right) \times \left(\frac{1+z}{6}\right)^3 \left(\frac{\Omega_b h_{50}^2}{0.08}\right)^2, \quad (1)$$

where $\bar{n}_{\rm H}(0)$ is the mean comoving number density of H atoms, $C \equiv \langle n_{\rm H\,II}^2 \rangle / \langle n_{\rm H\,II} \rangle^2$ is the H II clumping factor (angle brackets denote volume average over a suitably large volume that the average is globally meaningful), and the remaining symbols have their usual meanings. The origin of this formula is a simple photon counting argument, which indicates that in order to maintain ionization at a given redshift z, the number of ionizing photons emitted in a large volume of the universe multiplied by a characteristic recombination time, denoted $\bar{t}_{\rm rec}$, must equal the number of hydrogen atoms: $\dot{\mathcal{N}}_{\rm ion} \times \bar{t}_{\rm rec} = \bar{n}_{\rm H}(0)$. The clumping factor enters as a correction factor to account for the density inhomogeneities in the IGM induced by structure formation. We note that $\bar{t}_{\rm rec}$ is not the volume average of the local recombination time of the ionized plasma, as this would heavily weight regions with the longest recombination times; i.e., voids. A proper derivation of Equation (1) shows that $\bar{t}_{\rm rec} \propto \langle t_{\rm rec}^{-1} \rangle^{-1}$, which weights regions with the shortest recombination times, i.e., regions at the mean density and above.

Equation (1) is based on a number of simplifying assumptions discussed by Madau et al. (1999), including the assumption $\bar{t}_{\rm rec} \ll t$. It is this assumption that allows history-dependent effects to be ignored, and a quasi-instantaneous analysis of the photon budget for reionization to be performed. The validity of this assumption is naturally redshift-dependent, but it is also dependent upon the adopted definition of $\bar{t}_{\rm rec}$. A second comment about Equation (1) is that it does not ask how many ionizing photons per H atom are required to convert a neutral IGM to a fully ionized one, only how many are required to maintain the IGM in an ionized state. Because the recombination time is short at high redshifts, it is expected that this number is greater than one.

In this paper, we examine these and related topics within the context of a fully coupled numerical simulation of cosmic reionization based on a new flux-limited diffusion (FLD) radiation transport solver installed in the *Enzo* code (Norman et al. 2013; Bryan et al. 2014, hereafter Paper I). Our approach self-consistently couples all the relevant physical processes (gas dynamics, dark matter dynamics, self-gravity, star formation/feedback, radiative transfer, nonequilibrium ionization/recombination, heating and cooling) and evolves the system of coupled equations on the same high-resolution mesh. We refer to this approach as resolution matched, in contrast to previous approaches which decouple and coarse-grain the radiative transfer and ionization balance calculations relative to the underlying dynamical calculation. Our method is scalable with respect to the number of radiation sources, size of the mesh, and the number of computer processors employed. This scalability permits us to simulate cosmological reionization in large cosmological volumes ($L \sim 100$ comoving Mpc) while directly modeling the sources and sinks of ionizing radiation, including radiative feedback effects such as photoevaporation of gas from halos, Jeans smoothing of the IGM, and enhanced recombination due to small-scale clumping. In this paper, the first of several application papers, we investigate in a volume of modest size ($L = 20$ comoving Mpc) the mechanics of reionization from stellar sources forming in high-z galaxies, the role of gas clumping, recombinations, and the photon budget required to complete reionization.

By analyzing this simulation, we are able to critically examine the validity of Equation (1) as a predictor of when EoR will conclude, and we can calculate the integrated number of ionizing photons per H atom needed to ionize the simulated volume $\gamma_{\rm ion}/H = \int dt \dot{\mathcal{N}}_{\rm ion}/\bar{n}_{\rm H}(0)$. Ignoring recombinations within the virial radii of collapsed halos, we find $\gamma_{\rm ion}/H \approx 2$. We also examine whether modern revisions to Equation (1) using alternatively defined clumping factors (Pawlik et al. 2009; Raicevic & Theuns 2011; Finlator et al. 2012; Shull et al. 2012) are improvements over the original. We find that they systematically overestimate the redshift of reionization completion $z_{\rm reion}$ because the condition $\bar{t}_{\rm rec}/t \ll 1$ is never obeyed. We study the accuracy and validity of the time-dependent analytic model of Madau et al. (1999), and find that while it is in better agreement with the simulation, it also overestimates $z_{\rm reion}$ because it ignores important corrections to the ionization term at early and late times.

This paper is organized as follows. In Section 2, we discuss the design criteria for the simulation and briefly outline the basic equations and implementation of the FLD radiation transport model, referring the reader to Paper I for a more complete description of the numerical algorithms and tests. In Section 3, we present some general features of the simulation and demonstrate its broad consistency with observed star formation rate density and high-redshift galaxy luminosity function. In Section 4, we examine the accuracy of different clumping factor approaches to estimating the redshift of complete reionization. In Section 5, we derive a global estimate for the circumgalactic absorption of ionizing radiation from our simulation. In Section 6, we test a simple analytic model for the evolution of the ionized volume fraction $Q_{\rm H\,II}$ and present an improvement to the model which better agrees with our simulation. In Section 7, we discuss the implications of our results on the current understanding of reionization. Finally, in Section 8, we end with a summary of our main results and conclusions.

2. METHOD

2.1. Simulation Goals and Parameters

We use the *Enzo* code (Paper I), augmented with a FLD radiative transfer solver and a parameterized model of star formation and feedback (Norman et al. 2013) to simulate inhomogeneous hydrogen reionization in a 20 Mpc comoving box in a *WMAP7* ΛCDM cosmological model. We justify the use of FLD in Section 2.3 below. Details of the numerical methods and tests are provided in Paper I. Here we briefly describe the simulation's scientific goals and design considerations to put it into perspective with other reionization simulations. For completeness, the physical equations we solve and the treatment of the ionizing sources and radiation field are included below.

Our principal goal is to simulate the physical processes occurring in the IGM outside the virial radii of high-redshift galaxies in a representative realization of inhomogeneous reionization. We wish to simulate the early, intermediate, and

late phases of reionization in a radiation hydrodynamic cosmological framework so that we may study the nonequilibrium ionization/recombination processes in the IGM at reasonably high resolution self-consistently coupled to the dynamics. In this way, we can study such effects as optically thick heating behind the I fronts (Abel & Haehnelt 1999), Jeans smoothing (Shapiro et al. 1994; Gnedin 2000b), photoevaporation of dense gas in halos (Shapiro et al. 2004), and nonequilibrium effects in the low density voids. Because we carry out our simulation on a fixed Eulerian grid, we do not resolve the internal processes of protogalaxies very well. In this sense, our simulation is not converged on all scales. Nonetheless, Equations (2)–(7) are solved everywhere on the mesh self-consistently, including ionization/recombination and radiative transfer inside protogalaxies. The escape of ionizing radiation from galaxies to the IGM is thus simulated directly, and not introduced as a parameter. We use a star formation recipe that can be tuned to closely reproduce the observed high-z galaxy luminosity function, star formation rate density (SFRD), and redshift of reionization completion. This gives us confidence that we are simulating IGM processes in a realistic scenario of reionization.

We simulate a *WMAP7* (Jarosik et al. 2011) ΛCDM cosmological model with the following parameters: $\Omega_\Lambda = 0.73$, $\Omega_m = 0.27, \Omega_b = 0.047, h = 0.7, \sigma_8 = 0.82, n_s = 0.95$, where the symbols have their usual meanings. A Gaussian random field is initialized at $z = 99$ using the *Enzo* initial conditions generator *inits* using the Eisenstein & Hu (1999) fits to the transfer functions. The simulation is performed in a comoving volume of $(20\ \mathrm{Mpc})^3$ with a grid resolution of 800^3 and the same number of dark matter particles. This yields a comoving spatial resolution of 25 kpc and dark matter particle mass of $4.8 \times 10^5\ M_\odot$. This resolution yields a dark matter halo mass function that is complete down to $M_h = 10^8\ M_\odot$, which is by design, since this is the mass scale below which gas cooling becomes inefficient. However, due to our limited box size, our halo mass function is incomplete above $M_h \approx 10^{11}\ M_\odot$ (see Figure 4). In a forthcoming paper, we will report on a simulation of identical design and resolution as this one, but in a volume 64 times as large, which contains the rarer, more massive halos. With regard to resolving the diffuse IGM, our 25 kpc resolution equals the value recommended by Bryan et al. (1999) to converge on the properties of the Lyα forest at lower redshifts, is three times better than the optically thin high resolution IGM simulation described in Shull et al. (2012), and nearly four times better than the inhomogeneous reionization simulation described in Trac et al. (2008).

As described below in Section 2.4, we use a parameterized model of star formation calibrated to observations of high-redshift galaxies. The star formation efficiency parameter f_* is adjusted to match the observed star formation rate density in the interval $6 \leqslant z \leqslant 10$ from Bouwens et al. (2011a). The simulation consumed 255,000 core hours running on 512 cores of the Cray XT5 system *Kraken* operated by the National Institute for Computational Science at ORNL.

2.2. Governing Equations

The equations of cosmological radiation hydrodynamics implemented in the *Enzo* code used for this research are given by the following system of partial differential equations (Paper I):

$$\nabla^2\phi = \frac{4\pi g}{a}(\rho_b + \rho_{\mathrm{dm}} - \langle\rho\rangle), \tag{2}$$

$$\partial_t\rho_b + \frac{1}{a}\mathbf{v}_b\cdot\nabla\rho_b = -\frac{1}{a}\rho_b\nabla\cdot\mathbf{v}_b - \dot{\rho}_{\mathrm{SF}}, \tag{3}$$

$$\partial_t\mathbf{v}_b + \frac{1}{a}(\mathbf{v}_b\cdot\nabla)\mathbf{v}_b = -\frac{\dot{a}}{a}\mathbf{v}_b - \frac{1}{a\rho_b}\nabla p - \frac{1}{a}\nabla\phi, \tag{4}$$

$$\partial_t e + \frac{1}{a}\mathbf{v}_b\cdot\nabla e = -\frac{2\dot{a}}{a}e - \frac{1}{a\rho_b}\nabla\cdot(p\mathbf{v}_b) - \frac{1}{a}\mathbf{v}_b\cdot\nabla\phi + G - \Lambda + \dot{e}_{\mathrm{SF}} \tag{5}$$

$$\partial_t \mathrm{n_i} + \frac{1}{a}\nabla\cdot(\mathrm{n_i}\mathbf{v}_b) = \alpha_{\mathrm{i,j}}\mathrm{n_e}\mathrm{n_j} - \mathrm{n_i}\Gamma_{\mathrm{i}}^{ph}, \quad i = 1, \ldots, N_{\mathrm{s}} \tag{6}$$

$$\partial_t E + \frac{1}{a}\nabla\cdot(E\mathbf{v}_b) = \nabla\cdot(D\nabla E) - \frac{\dot{a}}{a}E - c\kappa E + \eta. \tag{7}$$

Equation (2) describes the modified gravitational potential ϕ due to baryon density ρ_{b} and dark matter density ρ_{dm}, where a is the cosmological scale factor, g is the gravitational constant, and $\langle\rho\rangle$ is the cosmic mean density. The collisionless dark matter density ρ_{dm} is evolved using the Particle Mesh method (equation not shown above), as described in Hockney & Eastwood (1988) and Paper I. Equations (3), (4), and (5) are conservation of mass, momentum, and energy, respectively, in a comoving coordinate system (Bryan et al. 1995, 2014). In the above equations, $\mathbf{v}_b \equiv a(t)\dot{\mathbf{x}}$ is the proper peculiar baryonic velocity, p is the proper pressure, e is the total energy per unit mass, and G and Λ are the heating and cooling coefficients, respectively. Equation (6) describes the chemical balance between the different ionization species (in this pape r, we used H I, H II, He I, He II, He III densities) and electron density. Here, $\mathrm{n_i}$ is the comoving number density of the i_{th} chemical species, $\mathrm{n_e}$ is the electron number density, $\mathrm{n_j}$ is the ion that reacts with species i, and $\alpha_{\mathrm{i,j}}$ are the reaction rate coefficient between species i and j (Abel et al. 1997; Hui & Gnedin 1997), and finally Γ_{i}^{ph} is the photoionization rate for species i.

2.3. Radiation Transport

Equation (7) describes radiation transport in the FLD approximation in an expanding cosmological volume (Reynolds et al. 2009; Norman et al. 2013). E is the comoving gray radiation energy density. The flux limiter D is a function of E, ∇E, and the opacity κ (Morel 2000), and has the form:

$$D = \mathrm{diag}\,(D_1, D_2, D_3)\,, \quad \text{where} \tag{8}$$

$$D_{\mathrm{i}} = c\left(9\kappa^2 + R_{\mathrm{i}}^2\right)^{-1/2}, \quad \text{and} \tag{9}$$

$$R_{\mathrm{i}} = \max\left\{\frac{|\partial_{\mathrm{x_i}}E|}{E}, 10^{-20}\right\}. \tag{10}$$

In the calculation of the gray energy density E, we assume $E_\nu(\mathbf{x}, t, \nu) = \tilde{E}(\mathbf{x}, t)\,\chi_E(\nu)$, therefore:

$$E(\mathbf{x}, t) = \int_{\nu_1}^{\infty} E_\nu(\mathbf{x}, t, \nu)\, d\nu = \tilde{E}(\mathbf{x}, t) \int_{\nu_1}^{\infty} \chi_E(\nu)\, d\nu, \quad (11)$$

which separates the dependence of E on coordinate $\mathbf{x}$ and time t from frequency ν. Here χ_E is the SED taken to be that of a Pop II stellar population similar to one from (Ricotti et al. 2002).

The validity and limitations of the FLD approximation to modeling the transport of ionizing radiation for cosmic reionization simulations is worthy of discussion. First note that within the FLD approximation, the radiative flux $\mathbf{F}$ is parallel to the gradient of the radiation energy density: $\mathbf{F} = -D\nabla E$. Therefore, radiation is guaranteed to propagate radially around a point source, as it should. Inside an ionized bubble, the gas is optically thin, and radiation streams radially at the speed of light toward the I front where it is absorbed. FLD reproduces this behavior precisely. In the limit that the opacity $\kappa \rightarrow 0$, the flux limiter D is formulated so that $\mathbf{F} \rightarrow cE\hat{e}_{\nabla E}$, where $\hat{e}_{\nabla E}$ is the unit vector in the direction of ∇E, a result that is easily verified from Equations (8)–(10). As a consequence of these two properties, FLD is able to faithfully reproduce the flow of radiation around isolated ionizing point sources. When FLD is coupled with an accurate ionization kinetics solver, our method accurately models the expansion of I fronts in uniform and stratified media (Paper I). Thus, in a cosmological reionization simulation, the early stages of I-front expansion are modeled accurately by our method when the H II regions are isolated.

As H II regions expand, there can be two occurrences: (1) H II regions from two or more isolated sources merge; and (2) I fronts sweep over dense, opaque clumps of gas casting a shadow behind them. Both of these occurrences create inhomogeneities and anisotropies in the radiation field. As FLD evolves the radiation energy density, which is the zeroth angular moment of the radiation intensity, it does not model anisotropies in the radiation field. It is therefore important to gauge the magnitude of the errors incurred in these two circumstances, and their impact on large scale reionization simulations. In Paper I, we document the performance of our method on two idealized test problems which address these two circumstances individually. We show that FLD obtains a shape and size for the consolidated H II region that is in better agreement to the adaptive ray tracing results of Wise & Abel (2011) than the results obtained using the variable tensor Eddington factor method of Petkova & Springel (2009), who first introduced the test problem. We note that none of the methods explicitly treat the transport of ionizing recombination radiation, which would be important to do for detailed comparisons. We also show that FLD accurately predicts the photoevaporation time of a dense blob despite the method's inability to cast a shadow. A qualitative difference between FLD and ray tracing occurs when an opaque cloud is being ionized from one side. Ray tracing will leave a small amount of neutral gas on the "night side" of the cloud due to self-shielding, whereas this neutral gas is not present in a FLD simulation since the cloud is illuminated from all sides once the I front has swept over the cloud.

Intuitively, these small scale inhomogeneities and anisotropies should become less important as overlap is approached and neutral gas is illuminated from multiple directions. To illustrate this, in the Appendix we compare FLD and ray tracing solutions on a scaled cosmological reionization test problem with identical mass and spatial resolution to the results presented in this paper. The ray tracing calculation is carried out using the adaptive ray tracing solver built into the *Enzo* code *Moray* (Wise & Abel 2011). We find that the FLD and Moray simulations are in good agreement with one another, with the FLD simulation ionizing slightly faster than the *Moray* simulation at early times but track one another at late times (Figure 32). A detailed comparison of phase diagrams reveals small differences in the H I fraction versus gas overdensity at early times which may be indicative of FLD ionizing gas of moderate overdensities too quickly. However, the temperature–density phase diagrams do not show this effect. Our conclusion, based on these analyses, is that despite small differences, both FLD and ray tracing predict similar evolutions for the gas and that any effects due to shadowing, or the lack thereof, are of minor consequence to the progress of the global ionization state.

2.4. Star Formation and Feedback

Because star formation occurs on scales not resolved by our uniform mesh simulation, we rely on a subgrid model which we calibrate to observations of star formation in high-redshift galaxies. The subgrid model is a variant of the Cen & Ostriker (1992) prescription with two important modifications as described in Smith et al. (2011). In the original Cen & Ostriker (1992) recipe, a computational cell forms a collisionless "star particle" if a number of criteria are met: the baryon density exceeds a certain numerical threshold; the gas velocity divergence is negative, indicating collapse; the local cooling time is less than the dynamical time; and the cell mass exceeds the Jeans mass. In our implementation, the last criterion is removed because it is always met in large-scale, fixed-grid simulations, and the overdensity threshold is taken to be $\rho_b/(\rho_{c,0}(1+z)^3) > 100$, where $\rho_{c,0}$ is the critical density at $z = 0$. If the three remaining criteria are met, then a star particle representing a large collection of stars is formed in that timestep and grid cell with a total mass

$$m_* = f_* m_{\rm cell} \frac{\Delta t}{t_{\rm dyn}}, \quad (12)$$

where f_* is an efficiency parameter we adjust to match observations of the cosmic SFRD (Bouwens et al. 2011a), $m_{\rm cell}$ is the cell baryon mass, $t_{\rm dyn}$ is the dynamical time of the combined baryon and dark matter fluid, and Δt is the hydrodynamical timestep. An equivalent amount of mass is removed from the grid cell to maintain mass conservation.

Although the star particle is formed instantaneously (i.e., within one timestep), the conversion of the removed gas into stars is assumed to proceed over a longer timescale, namely $t_{\rm dyn}$, which more accurately reflects the gradual process of star formation. In time Δt, the amount of mass from a star particle converted into newly formed stars is given by

$$\Delta m_{\rm SF} = m_* \frac{\Delta t}{t_{\rm dyn}} \frac{t - t_*}{t_{\rm dyn}} e^{-(t-t_*)/t_{\rm dyn}}, \quad (13)$$

where t is the current time and t_* is the formation time of the star particle. To make the connection with Equation (4), we have $\dot{\rho}_{\rm SF} = \Delta m_{\rm SF}/(V_{\rm cell}\Delta t)$, where $V_{\rm cell}$ is the volume of the grid cell.

Stellar feedback consists of the injection of thermal energy, gas, and radiation to the grid, all in proportion to $\Delta m_{\rm SF}$. The thermal energy $\Delta e_{\rm SF}$ and gas mass Δm_g returned to the grid are given by

$$\Delta e_{\rm SF} = \Delta m_{\rm SF} c^2 \epsilon_{\rm SN}, \qquad \Delta m_g = \Delta m_{\rm SF} f_{m*}, \quad (14)$$

where c is the speed of light, $\epsilon_{\rm SN}$ is the supernova energy efficiency parameter, and $f_{m*} = 0.25$ is the fraction of the stellar mass returned to the grid as gas. Rather than add the energy and gas to the cell containing the star particle, as was done in the original Cen & Ostriker (1992) paper, we distribute it evenly among the cell and its 26 nearest neighbors to prevent overcooling. As shown by Smith et al. (2011), this results in a star formation recipe which can be tuned to reproduce the observed SFRD. This is critical for us, as we use the observed high-redshift SFRD to calibrate our reionization simulations.

To calculate the radiation feedback, we define an emissivity field $\eta(x)$ on the grid which accumulates the instantaneous emissivities $\eta_i(t)$ of all the star particles within each cell. To calculate the contribution of each star particle i at time t, we assume an equation of the same form for supernova energy feedback, but with a different energy conversion efficiency factor $\epsilon_{\rm UV}$. Therefore,

$$\eta = \sum_{\rm i} \epsilon_{\rm uv} \frac{\Delta m_{\rm SF} c^2}{V_{\rm cell} \Delta t} \tag{15}$$

Emissivity η is in units of erg s^{-1} cm^{-3}. The UV efficiency factor $\epsilon_{\rm uv}$ is taken from Ricotti et al. (2002) as $4\pi \times 1.1 \times 10^{-5}$, where the factor 4π comes from the conversion from mean intensity to radiation energy density. We note that Equation (15) as written absorbs the customary ionizing escape fraction parameter into $\epsilon_{\rm UV}$, and that since we are using an unattenuated value for $\epsilon_{\rm UV}$ we are in effect assuming $f_{\rm esc}({\rm ISM}) = 1$. However, the results of our simulation would be identical if we had chosen a more realistic value for the escape fraction, and adjusted the intrinsic emissivity upward to compensate, so as to obtain the same redshift of reionization completion.

2.5. Data Analysis

Due to the enormous amount of data produced by the simulation (one output file is about 100 GB), we needed a scalable tool suited to the task of organizing and manipulating the data into human readable form. We use the analysis software tool `yt` (Turk et al. 2011) specifically created for doing this type of vital task. It is a python-based software tool that performs "Detailed data analysis and visualizations, written by working astrophysicists and designed for pragmatic analysis needs" (http://icer.msu.edu/software-highlights/yt-project) `yt` is open source and publicly available at http://yt-project.org.

3. GENERAL RESULTS

Here we first present the basic properties of the simulation before delving into specific topics in subsequent sections. The star formation and feedback parameters for this simulation are $f_* = 0.1$, $f_{m*} = 0.25$, $\epsilon_{\rm SN} = 10^{-5}$, and $\epsilon_{\rm UV} = 1.38 \times 10^{-4}$. Figure 1 shows the reionization process as it proceeds through the growth, percolation, and final overlap of ionized hydrogen (H II) regions driven by ionizing radiation from star-forming galaxies. We plot the neutral hydrogen (H I) density on a slice through the densest cell in the volume at redshifts $z = 9.18, 8.0, 7.0, 6.1$. At $z = 9.18$ several isolated quasi-spherical I fronts are intersected by the slice plane. These grow and have begun to merge by $z = 8.0$. By $z = 7.0$ the topology is beginning to invert, in that there are now isolated peninsula of H I gas embedded in an otherwise ionized IGM. By $z = 6.1$ the remaining neutral island has almost disappeared as it is being irradiated from all sides. We can also see in the figure small patches of extremely low H I density; these correspond to bubbles of shock-heated gas near galaxies heated to above 10^6 K in temperature by supernova feedback.

Figure 2 plots the evolution of the ionized volume fraction $Q_{\rm H\,II}$ versus redshift. Here a cell is considered to be ionized if $\rho_{\rm H\,II}/\rho_{\rm H} \geqslant 0.999$ (In Section 3.1 we discuss the sensitivity of this curve to level of ionization.) The first ionizing sources turn on at $z \sim 10$ in this simulation. The ionized volume fraction rises rapidly, reaching 0.5 at $z \approx 6.8$, 0.95 at $z \approx 6.0$, and near unity at $z \approx 5.8$. We compare this evolution with the predictions of the simple analytic model introduced by Madau et al. (1999) in Section 6. For now, we only draw attention to the flattening of the curve in the redshift interval $5.8 \leqslant z \leqslant 6$. This is the signature of neutral islands being ionized by I fronts converging in three dimensions (3D), as opposed to being ionized by internal sources.

Our simulation was not designed to complete reionization by a certain fiducial redshift. Rather, we adjusted our star formation efficiency parameter f_* so that we can approximately match the SFRD in (Bouwens et al. 2011a). Our SFRD is shown in Figure 3, along with the Bouwens data, plotted without error bars. This shows that our simulated universe is one that produces approximately the same amount of stars in a given comoving volume, albeit a bit low relative to the data. We also note that the SFRD begins to flatten out at $z \approx 6.5$, and even turns over after overlap at $z \approx 5.8$, rather than continue to rise as indicated by the data points. This is an artifact of the small box size as a simulation completed in a 80 Mpc comoving on a side box with identical physics, mass, and spatial resolution and star formation/feedback parameters does not show this slowing down of the SFRD. This will be reported on in a future paper.

To check whether our simulation is giving us a fair representation of the universe, we plot several more quantities and look for any anomalies. In Figure 4, we see that our halo mass function at redshift of $z \sim 6$ matches well with the Warren fit implemented in `yt` (Warren et al. 2006; Turk et al. 2011). The mass function captures halos down to $\sim 10^8\ M_\odot$, which, as previously stated, was a simulation design criterion. The halos are found by first running the parallelHOP halo finder installed in `yt` (Skory et al. 2010), then taking the linked list of dark matter particles for each halo and wrapping the region around them in an ellipsoidal 3D container introduced in `yt` 2.4. The 3D container enables the query of the fluid quantities of the halos, such as baryonic, emissivity, and radiation contents, in addition to the particle information. Since the dark matter particles used are $\sim 5 \times 10^5\ M_\odot$, the $10^8\ M_\odot$ dark matter halos are considered to be resolved (Trenti et al. 2010).

As a final check that our ionizing source population is not wildly unrepresentative of the observed universe, in Figure 5 we plot the luminosity function of our simulated galaxies at $z = 6.1$ alongside the observational data points from Table 5 of Bouwens et al. (2007). The points in red are the bolometric luminosities for our galaxy population calculated directly from the $z = 6.1$ halo catalog. To calculate the luminosity of a given halo, we sum the emissivity field within the 3D ellipsoidal containers defined by the halos' dark matter particles. Our error bars are taken using one standard deviation of luminosity in the mass bins. Although this is not proof that our simulation is matching observations exactly, it does lend support that our realization of reionization is being driven by sources not too dissimilar to those observed and is sufficient for the purposes of this study.

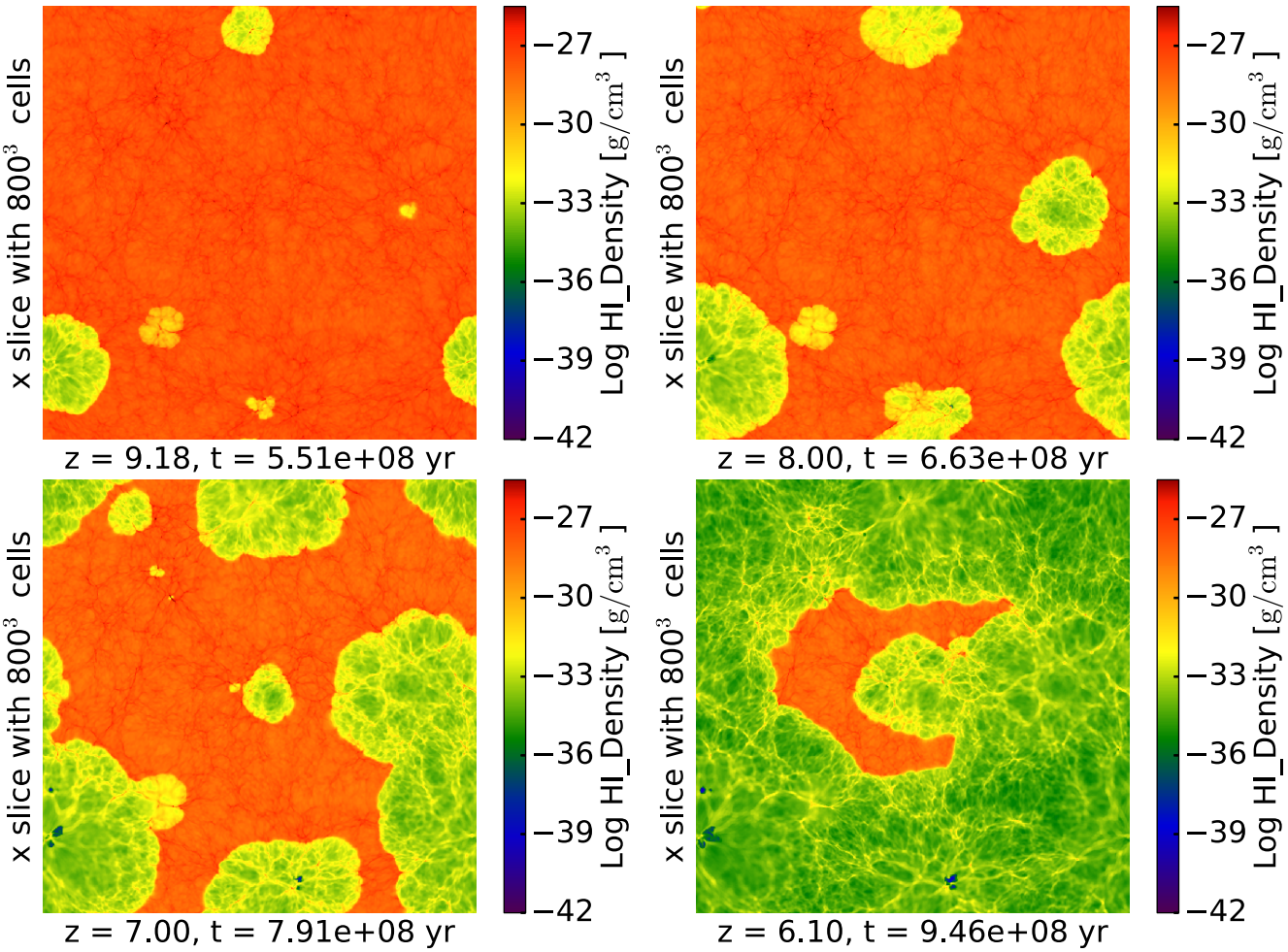

Figure 1. H I density on slices through the 20 Mpc volume showing the growth, percolation, and final overlap of H II regions. Panels show $z = 9.18$, 8.0, 7.0, and 6.1. The box becomes fully ionized at $z = 5.8$ as the last neutral islands are overrun by the I fronts. Regions of extremely low H I density are shock-heated bubbles due to supernova feedback.

(A color version of this figure is available in the online journal.)

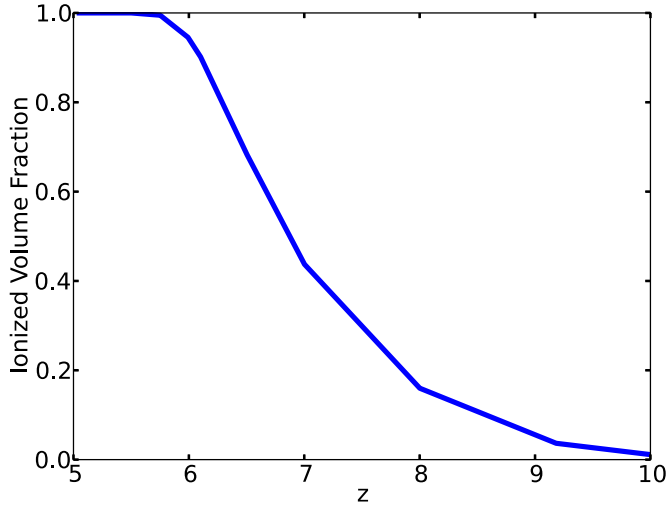

Figure 2. Evolution of the ionized volume fraction vs. redshift for hydrogen ionized to less than one neutral in 10^3 atoms. As redshift decreases, the volume filling fraction grows rapidly until around redshift of 6, at which time the rate of growth slows significantly as the last neutral island is ionized. The sensitivity of this curve to the ionization level is discussed in Section 3.1.

(A color version of this figure is available in the online journal.)

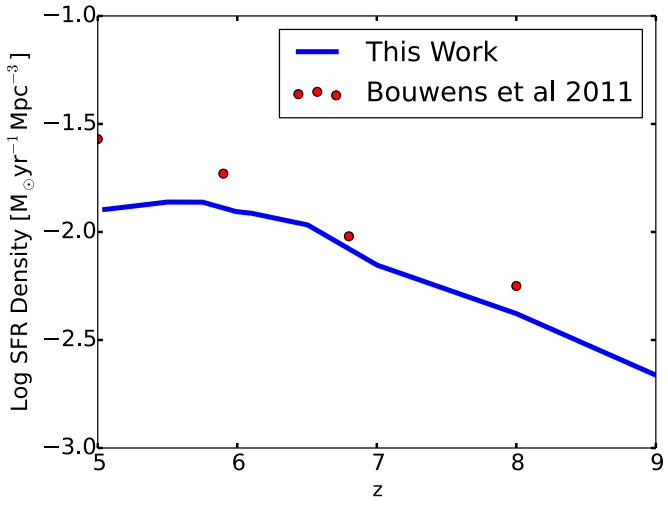

Figure 3. Comparison of simulated and observed star formation rate densities (SFRD) in units of $M_\odot$ yr^{-1} Mpc^{-3} comoving. The blue curve labeled "This Work" is from our 20 Mpc/800^3 simulation, and "Bouwens et al. (2011)" are observationally derived data points from Bouwens et al. (2011b) plotted without error bars. The leveling off of the simulated SFRD is an artifact of the small volume as a simulation carried out with identical physics, mass, and spatial resolution but in 64 times the volume does not show this effect.

(A color version of this figure is available in the online journal.)

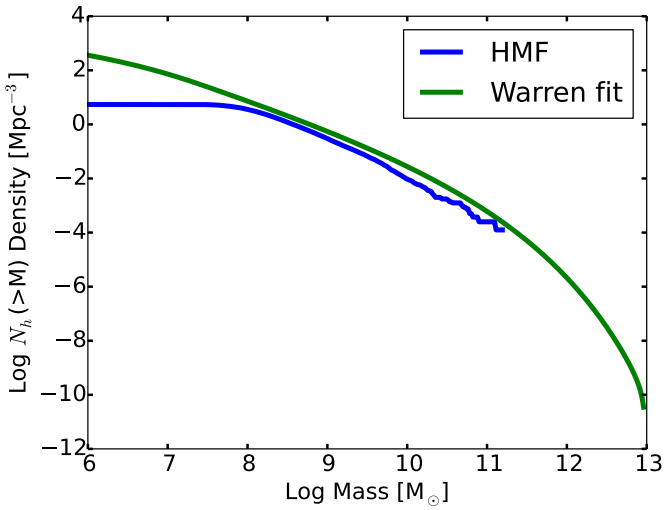

Figure 4. Dark matter halo mass function from our simulation (blue line). The green line is the fit from (Warren et al. 2006). Our low-mass halo mass function (HMF) is reasonably complete down to $M_{\rm halo} \approx 10^8\,M_\odot$; i.e., halos believed to form stars efficiently due to atomic line cooling. Incompleteness at the high-mass end is due to the limited volume sampled.

(A color version of this figure is available in the online journal.)

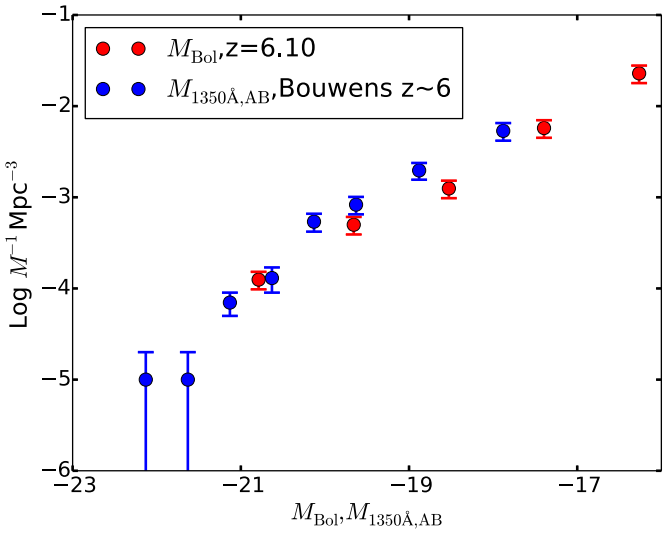

Figure 5. Bolometric luminosity function derived from our simulation data (red), compared with observational data points (blue) from Bouwens et al. (2007).

(A color version of this figure is available in the online journal.)

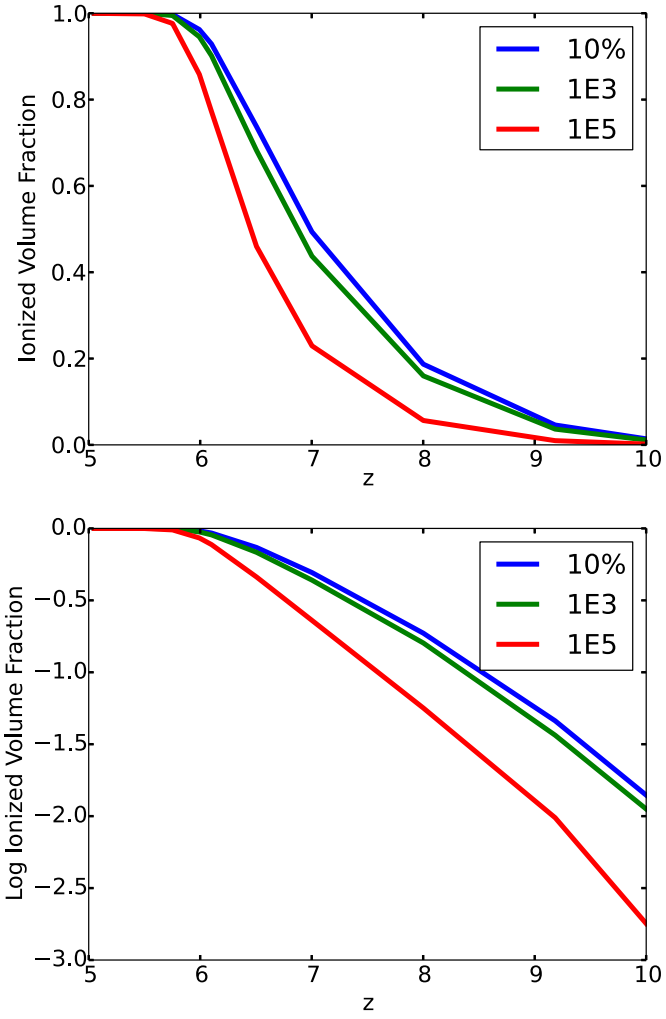

Figure 6. Volume filling fraction of ionized gas vs. redshift for three ionized fraction thresholds. Top: linscale. Bottom: logscale. The three ionization levels are "10%" in blue: fractional volume that have more than 1 ionized hydrogen atom per 10 hydrogen atoms. "1E3" in green: fractional volume that have less than 1 neutral hydrogen atom per 10^3 hydrogen atoms. "1E5" in red: fractional volume that have less than 1neutral hydrogen atom per 10^5 hydrogen atoms.

(A color version of this figure is available in the online journal.)

3.1. Quantitative Language

Earlier works on reionization such as Valageas & Silk (1999), Gnedin (2000a), and Miralda-Escudé et al. (2000), Iliev et al. (2006) speak of a two-phase medium composed of completely neutral and completely ionized hydrogen gas, while more recent works (Ciardi et al. 2003; Zahn et al. 2007; Shin et al. 2008; Petkova & Springel 2011; Finlator et al. 2012) begin to consider the degree of ionization within ionized gas. The simplification of considering a two-phase medium helps reduce the simulation complexity and the language needed to describe the results. However, as simulations become more sophisticated, the two-phase paradigm becomes ill-suited to convey the wealth of information contained in the larger and more detailed simulations. New simulations are described, the old paradigm lingers and causes ambiguities. As a case in point, consider the ionized volume filling fraction versus redshift, one of the simplest quantitative metrics of any reionization simulation. Within the framework of a two-phase medium, this is uniquely defined at any redshift. For a simulation such as ours which tracks the ionization state in every cell, the volume filling fraction depends on the degree of ionization, as illustrated in Figure 6.

This figure shows the evolution of the volume filling fraction of ionized gas which exceeds a minimum local ionization fraction $f_i \equiv \rho_{\rm H\,II}/\rho_{\rm H}$. The three thresholds are $f_i = 0.1, 0.999$, and 0.99999 and are labeled 10%, 1E3, 1E5, respectively in Figure 6. We choose three specific levels not because we believe that they are more important than others, but because it suits our later narrative and gives a range of values. With the ionization state tracked by the simulation, we see that it is now ambiguous to ask at what redshift 50% of the volume is ionized. In our simulation, this occurs at $z \approx 7$, 6.8 and 6.5 for $f_i = 0.1$, 0.999, and 0.99999, respectively.

In the remainder of this paper, we will often report results as a function of these three ionization fraction thresholds. To make the text easier to read, we will use the terms "Ionized" to

designate $f_i = 0.1$, "Well Ionized" to designate $f_i = 0.999$, and "Fully Ionized" to designate $f_i = 0.99999$ ionization levels.

3.2. Inside-out or Outside-in

Besides specifying the amount of ionized volume and levels of ionization, another area where quantitative language is useful is in the description of the reionization history. Since the Outside-in model was proposed by Miralda-Escudé et al. (2000), there is support gathering for the opposing view of the Inside-out model by Sokasian et al. (2003), Furlanetto et al. (2004), and Iliev et al. (2006), to name a few. In Finlator et al. (2009), the authors go even further and add to the lexicon "Inside-outside-middle," trying to describe the rich details of a reionization scenario. The basic Inside-out picture is that galaxies form in the peaks of the dark matter density field and drive expanding H II regions into their surroundings (expansion phase). These H II regions are initially isolated, but begin to merge into larger, megaparsec-scale H II regions due to the clustering of the galaxy distribution (percolation phase). Driven by a steadily increasing global star formation rate and recombination time (due to cosmic expansion) this process goes on until H II regions completely fill the volume (overlap phase). In this picture, rare peaks in the density field ionize first while regions of lower density ionize later from local sources that themselves formed later.

To investigate how reionization progresses in regions of different density, in Figure 7 we plot the hydrogen neutral fraction ($\rho_{\rm H\,I}/\rho_{\rm H}$) versus overdensity $\Delta_b \equiv \rho_b/\langle\rho_b\rangle$ in the left column, and in the right column a slice of the gas temperature, with redshift decreasing from top to bottom. One would expect that if inside-out ionization is the case, the neutral fraction of higher density region should drop down more quickly than lower density regions. Below, we will describe each row of the figure in more detail.

Looking at the redshift $z = 10$ row, we see in the gas temperature slice that two isolated regions of ionization appear due to UV feedback from new stars, indicated by the $\sim 10^4$ K gas. These regions correspond to places on the neutral fraction versus overdensity phase plot where a small amount of volume emerges around Δ_b of 10^{-1}–10^1, reaching Well Ionized to Fully Ionized levels. The $T \sim 10^7$ K region corresponds to the extended tail of very low neutral fraction gas in the left column, and indicates gas shock heated by supernova feedback. Although the cell count of shock heated gas will grow, it remains orders of magnitude smaller compared to the photoionized regions that we will emphasize. Even at this early stage, there are high-density regions above Δ_b of 10^2–10^3 that are Well Ionized; this is due to their close proximity to the ionizing sources, supporting the Inside-out paradigm.

Looking at the next row of figures at a redshift of $z = 7$, we see that the volume of Well Ionized regions has increased greatly, and so has the shock heated region in the phase plot. We also see that most, but not all, of the $\Delta_b > 10^2$ cells have reached the Well Ionized level. Although a large portion of the volume is in the Well Ionized regime, the majority of the volume (the red pixels) is still neutral, as we can see in the corresponding temperature slice plot. Most of the volume is still well under 10^4 K, where we expect the temperature to hover around once the ionization front has passed through the region and the gas has had time to come into photoionization thermal equilibrium.

By a redshift of $z = 6.1$, we see from the left column that the region that is ionized beyond the Fully Ionized level (an irony in terms, which means there is definitely room for improvement in the naming convention), dominates the simulation volume. There are still some regions not yet consumed by the ionization front, which is seen on the top of the neutral fraction plot and on the right according to the temperature slice.

The next row at redshift of $z = 5.5$ is after the entire volume has been swept over by ionization fronts. Most of the volume is beyond the Well Ionized level, except for a few cells around $\Delta_b \sim 10^2$. There are also some cells that are still neutral around $\Delta_b \sim 10^4$. They remain neutral because their densities are so high, leading to high recombination rates. Over time, these cells will shift up and down the neutral fraction plot with waves of star formation and supernova explosions since they are likely close to the source of the radiation and kinetic energy.

The last row of Figure 7 is at redshift $z \sim 5$, where we can see that the previous few cells that have yet to reach Well Ionized levels around $\Delta_b \sim 10^2$–10^3 have now disappeared. The cells that have not reached Well Ionized level before are cells where either the radiation is not strong enough due to shielding effects or the density is so high the gas recombines quickly even after being ionized. After the ionization front has passed through and highly ionized the IGM, there is little material left to shield against the radiation background and we see all but the densest few cells become Well Ionized. The high-density region reaching the same ionization level after the under dense void would fit well with the description for the Outside-in model. Note that the remaining cells that finally reached Well Ionized levels are orders of magnitude smaller in total volume compare to the rest of the cells at the same density. So if we call cells of $\Delta_b \sim 10^2$ filaments, not all dense filaments get Well Ionized until late in the EoR. Before the volume is filled with radiation, these dense filaments are able to remain relatively neutral.

Unfortunately, the evolution of these redshift panels is not enough to capture the propagation of radiation fronts from the initial sources, but they do convey the overall ionization history of the universe. The panels suggest that the region surrounding the ionization sources, whether they are dense cores, filaments, or voids, are all affected by the radiation on roughly the same timescale. However, the degree to which they are ionized is different. It is this difference that is the key to answering the original question, whether the universe ionize inside-out or outside-in.

When focusing on the ionization of the IGM, for a moment let us neglect the $\Delta_b \sim 10^4$ cells that shift ionization level with waves of star formation which comprise a very small fraction of the volume. If we use the "Ionized" level to characterize something as completely ionized and draw the line for neutral fraction at 10%, then the universe reaches end of EoR before $z \sim 5.5$. Since radiation propagates from sources outward, that would correspond to the Inside-out picture. If we were to instead draw the completely ionized line at the "Well Ionized" level, then we can see that even at $z \sim 5.5$, there is a small peak in the dense region of the phase diagram ($\Delta_b \sim 2.4 \times 10^2$) that has yet to reach below the line to be considered completely ionized. This would correspond to the Outside-in picture which reaches end of EoR sometime before $z \sim 5$ (or Inside-outside-middle if one uses the Finlator et al. 2009 terminology and considers the neutral peak to be a part of the filaments). Finally, if we were to draw the line at the "Fully Ionized" level, the universe has yet to ionize even for regions that are only 10 times overdense. Thus, the ionization history is a story with many perspectives, and it really depends on how the story teller draws the line as to whether Inside-out, Outside-in, or Inside-outside-middle is a better qualitative description.

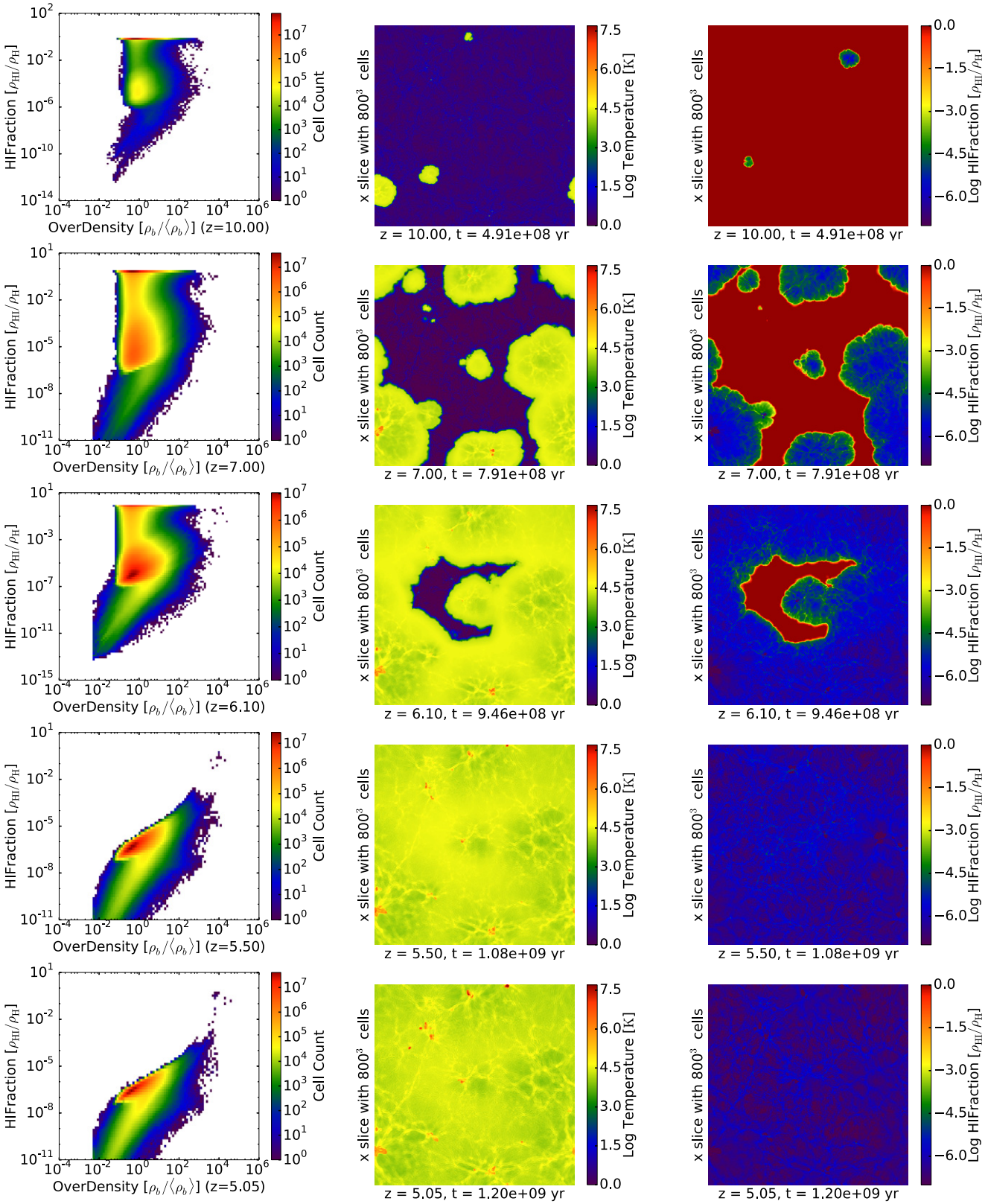

Figure 7. Left: phase diagram of neutral hydrogen fraction versus baryon overdensity with decreasing redshift from top to bottom. Middle: slices of Log Temperature [K] through a region that remained mostly neutral until just before overlap at redshift of ~5.8. Right: slices of neutral hydrogen fraction through the same region as before. Please refer to Section 3.2 for detailed description.

(A color version of this figure is available in the online journal.)

4. CLUMPING FACTORS AND THE PHOTON BUDGET FOR REIONIZATION

4.1. Clumping Factor Analysis of Madau

In this section, we begin our examination of Equation (1) from Madau et al. (1999) as an accurate predictor of when reionization completes, focusing on the clumping factor. The evolution of the three clumping factors is shown in Figure 9. While it is true that the Madau-type analysis was not designed to predict the precise redshift for reionization completion, only the ionization rate density needed to maintain the IGM in an ionized state after reionization has completed, it is effectively being used in this way when it is applied to galaxy populations at increasingly higher redshifts $z = 6$–7 (see Fan et al. 2006; Robertson et al. 2013). Our methodology is as follows. The simulation supplies $\dot{N}_{\rm sim}(z)$ ionizing photons, which increases with decreasing redshift because the SFRD increases with decreasing redshift. Equation (1) poses a minimum requirement on the ionizing emissivity to maintain the IGM in an ionized state at given redshift z. This requirement decreases with decreasing redshift due to the strong z dependence. We look to see if the box becomes fully ionized when these two curves cross; i.e., when $\dot{N}_{\rm sim} \geqslant \dot{\mathcal{N}}_{\rm ion}$. In subsequent sections, we do this for more recent definitions of the clumping factor that have been introduced by various authors in roughly chronological order.

The clumping factor is introduced and used to estimate the amount of recombination that radiation has to overcome in order to keep the universe ionized (Gnedin & Ostriker 1997; Valageas & Silk 1999; Madau et al. 1999; Fan et al. 2006). In a homogeneous universe, the hydrogen recombination rate is also homogeneous, and is a simple function of the mean density, ionization fraction, and temperature. The clumping factor is a correction factor to account for density inhomogeneities induced by structure formation, although, in principle, inhomogeneities in ionization fraction and temperature are also important. The most common definition for the clumping factor is

$$C = \frac{\langle n_{\rm H\,II}^2 \rangle}{\langle n_{\rm H\,II} \rangle^2}, \tag{16}$$

where the $\langle\rangle$ brackets denote an average over the simulation volume. To see where this comes from, let us look at the change of $n_{\rm H\,II}$ with respect to time due to recombinations:

$$\begin{aligned}
\frac{\partial n_{\rm H\,II}}{\partial t} &= -n_{\rm e} n_{\rm H\,II} \alpha_B(T) \\
\frac{\partial n_{\rm H\,II}}{n_{\rm H\,II}} &= -\partial t n_{\rm e} \alpha_B(T) \\
\int_{n_i}^{n_f} \frac{\partial n_{\rm H\,II}}{n_{\rm H\,II}} &= -\int_{t_i}^{t_f} \partial t n_{\rm e} \alpha_B(T) \\
\ln\left(\frac{n_f}{n_i}\right) &= -(t_f - t_i) n_{\rm e} \alpha_B(T), \\
\frac{n_f}{n_i} &= \exp(-t_{\rm rec} n_{\rm e} \alpha_B).
\end{aligned} \tag{17}$$

In the last step, we have set $(t_f - t_i)$ to be $t_{\rm rec}$. This leads to

$$t_{\rm rec} = [n_{\rm e} \alpha_B(T)]^{-1} \tag{18}$$

being the characteristic time when the fraction $n_f/n_i = 1/e$. Using this expression for the recombination time, one can rewrite the right-hand side of the equation as

$$\begin{aligned}
\frac{\partial n_{\rm H\,II}}{\partial t} &= -n_{\rm H\,II} n_{\rm e} \alpha_B(T) = -n_{\rm H\,II}/t_{\rm rec} \\
&= -n_{\rm H\,II}(1 + 2\chi) n_{\rm H\,II} \alpha_B(T) \\
&= -n_{\rm H\,II}^2 (1 + 2\chi) \alpha_B(T),
\end{aligned} \tag{19}$$

where, in the last two steps, following Madau et al. (1999), we replace $n_{\rm e}$ with $(1 + 2\chi) n_{\rm H\,II}$ assuming helium is fully ionized. Here χ is the cosmic fraction of helium. Taking the volume average, we have:

$$\begin{aligned}
\left\langle \frac{\partial n_{\rm H\,II}}{\partial t} \right\rangle &= -\left\langle n_{\rm H\,II}^2 (1 + 2\chi) \alpha_B(T) \right\rangle \\
&= -\left\langle n_{\rm H\,II}^2 \right\rangle (1 + 2\chi) \alpha_B \\
&= -\langle n_{\rm H\,II} \rangle^2 (1 + 2\chi) \alpha_B C \\
&= -\langle n_{\rm H\,II} \rangle / \bar{t}_{\rm rec}.
\end{aligned} \tag{20}$$

In the above, we have made the oft-used assumption of a uniform IGM temperature of 10^4 K, making the Case B recombination coefficient, α_B a constant. Note this is not physically justified, but since the temperature of the IGM is not well determined observationally, it is a useful approximation, and one that is embedded in Equation (1). With this simplifying assumption, when taking the volume average on both sides of the equation, we may rewrite the result in the same form as the first line in Equation (19). Therefore, the effective recombination time can be written as

$$\bar{t}_{\rm rec} = t_{\rm Madau} \equiv [(1 + 2\chi) \langle n_{\rm H\,II} \rangle \alpha_B C]^{-1}. \tag{21}$$

This expression is the same as Equation (20) of Madau et al. (1999) if we substitute $\langle n_{\rm H\,II} \rangle$ for $\bar{n}_{\rm H}$. In the case of a fully ionized universe, these two quantities are equivalent. We note that $t_{\rm Madau}$ is not at all the volume average of $t_{\rm rec}$ but is $\langle t_{\rm rec}^{-1} \rangle^{-1} C^{-1}$, which weights regions with the shortest recombination times; i.e., regions at the mean density and above. If we now make the *ansatz* $\dot{\mathcal{N}}_{\rm ion} \times \bar{t}_{\rm rec} = \bar{n}_{\rm H}(0)$, we may derive Equation (26) in Madau et al. (1999), updated by Fan et al. (2006), repeated here for convenience:

$$\dot{\mathcal{N}}(z) = 10^{51.2}\ {\rm s}^{-1}\ {\rm Mpc}^{-3} \left(\frac{C}{30}\right) \left(\frac{\Omega_{\rm b} h^2}{0.02}\right)^2 \left(\frac{1+z}{6}\right)^3. \tag{22}$$

This equation gives an estimate of the ionizing photon production rate density (in units of ${\rm s}^{-1}$ ${\rm Mpc}^{-3}$ comoving) that is needed to balance the recombination rate density (the right-hand side of Equation (22)) in a completely ionized universe. Values for C ranging $\sim$10–30 are often quoted from earlier hydrodynamical simulations such as Gnedin & Ostriker (1997), and $\sim$3 for more recent work following Pawlik et al. (2009), Raicevic & Theuns (2011), Shull et al. (2012), Finlator et al. (2012) and the methods there.

We follow these earlier studies using our own simulation data. In Figure 8, we plot the ionizing photon production rate density and recombination rate density from our fiducial simulation. The curve in blue labeled $\dot{N}_{\rm sim}$ is the photon production rate density from the simulation, calculated using a time average of the volume integrated ionizing emissivity η (Equation (15)) divided by the average energy per photon which we obtain directly from the SED. The other three curves plot Equation (22) for three methods for calculating C: green uses the H II density directly

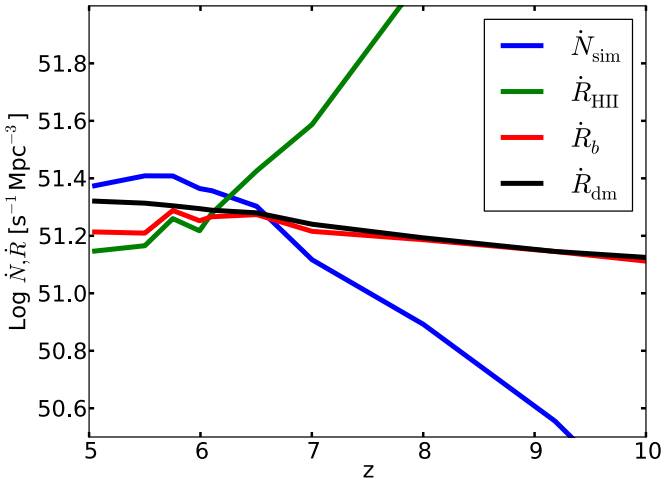

Figure 8. Ionizing photon production rate density and various estimates of the recombination rate density vs. redshift. The blue curve labeled "$\dot{N}_{\rm sim}$" is the measured photon production rate density averaged over the entire simulation volume. The green curve labeled "$\dot{R}_{\rm H\,II}$" is the recombination rate density estimate from using the clumping factor calculated with Equation (16) substituted in Equation (22). The red curve labeled "$\dot{R}_b$" is Equation (22) evaluated using a clumping factor calculated from the baryon density. The black curve labeled "$\dot{R}_{\rm dm}$" is using a clumping factor calculated with dark matter density.

(A color version of this figure is available in the online journal.)

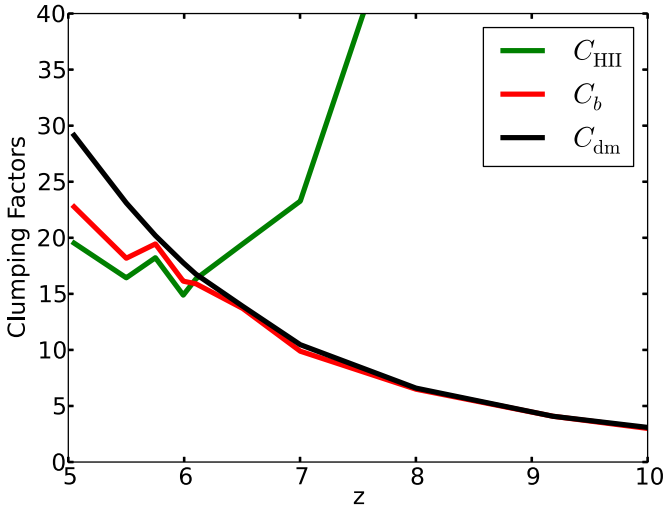

Figure 9. Unthresholded clumping factors used in Figure 8. $C_{\rm H\,II}$, C_b, C_{dm} are calculated from the unthresholded H II, baryon, and dark matter densities, respectively.

(A color version of this figure is available in the online journal.)

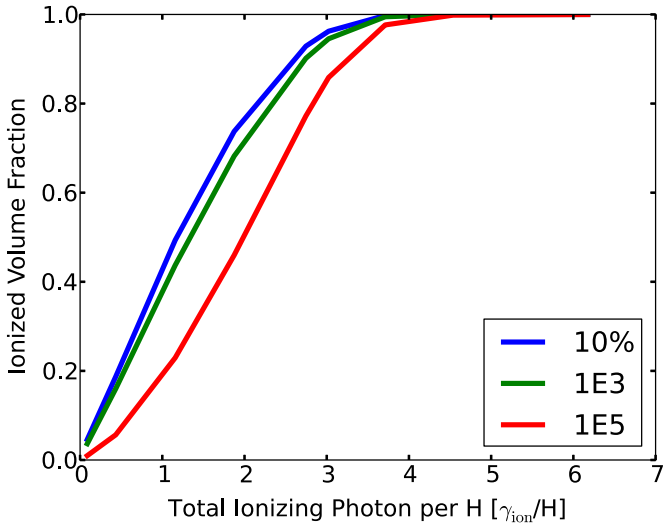

Figure 10. Ionized volume fraction as a function of the number of ionizing photons emitted per H atom averaged over the entire simulation volume (including inside halos) for three different ionization levels: $f_i \geqslant 0.1$ (blue line); $f_i \geqslant 0.999$ (green line); $f_i \geqslant 0.99999$ (red line). Compare with Figure 14, which excludes gas inside halos.

(A color version of this figure is available in the online journal.)

(Equation (16)); red uses the baryon density $C = \langle\rho_b^2\rangle/\langle\rho_b\rangle^2$; and black uses the dark matter density $C = \langle\rho_{dm}^2\rangle/\langle\rho_{dm}\rangle^2$. In all cases no thresholding is being applied (the effect of thresholding is examined in the next section); the averages are done over every cell in the simulation including those inside the virial radii of galaxies. The H II curve drops sharply with decreasing redshift because C is large when the H II distribution is patchy. The baryon and dark matter curves track one another for $z > 6$ because the clumping factors are nearly the same, but begin to separate after overlap as the baryon clumping factor drops due to Jeans smoothing.

Where the ionization and recombination rate density lines cross is roughly when we expect the universe to become highly ionized. If we define the end of the EoR as when 99.9% of the volume has reached the Well Ionized level, then our simulation reaches that point around $z \sim 5.8$ according to Figure 6. The $\dot{N}_{\rm sim}$ curve crosses the $\dot{R}_{\rm H\,II}$ curve at $z \sim 6.2$. This is somewhat reassuring since we are counting every ionizing photon emitted and every recombination, at least insofar as Equation (22) provides a good estimate of that. The recombination rate density curves using clumping factors computed from the baryon and dark matter densities curves cross the $\dot{N}_{\rm sim}$ curve at a somewhat higher redshift of $z \approx 6.6$. By following the original methodology of using the clumping factor to estimate recombinations, we find that the clumping factor calculated with the H II density field to be the closest predictor for the end of EoR in our simulation.

The photon budget that enabled us to reach different levels of ionization is plotted in Figure 10. Here we plot the evolution of the ionized volume fraction versus $\gamma_{\rm ion}/H = \int dt \dot{N}_{\rm sim}/\bar{n}_{\rm H}(0)$. So, adopting the same definition for the end of EoR, we see that we need ~four photons per hydrogen atom to achieve it. This cannot be considered a converged result because this estimate includes the dense gas inside galaxies, which is not well resolved in our simulation. Even though a small fraction of the baryons reside inside galaxies, due to the short recombination time, many ionizing photons are required to keep the gas ionized. Since we have not resolved the internal structure of galaxies, and higher resolution would likely result in higher density gas, we must consider $\gamma_{\rm ion}/H = 4$ a lower bound. We eliminate this issue in the next subsection by excluding the dense gas in halos from the calculation.

4.2. Quantitative Analysis of Recombinations

As the clumping factor method grew in popularity, various authors have applied thresholds of one form or another to improve upon its accuracy in predicting the recombination rate density needed to maintain an ionized universe. When thresholds are applied, parts of the volume are excluded from the photon counting analysis. Pawlik et al. (2009), Raicevic & Theuns (2011) and others limit the calculation of the clumping factor to the low density IGM by using Δ_b thresholds, usually set at

100. They threshold out gas in virialized halos and the self-shielded collapsed objects because radiation does not penetrate these objects, or they recombine too fast, which leaves them neutral and not contributing to recombinations in the IGM. More recently, Shull et al. (2012) has also thresholded out void regions ($\Delta_b < 1$), arguing that they do not contribute appreciably to the total recombinations due to their long recombination times.

To investigate the contribution of gas of different density to the total recombination rate density, in Figure 11, we plot three quantities dealing with recombinations in our simulation. In the left column,we have a two-dimensional (2D) distribution plot of recombination rate density $\dot{R} = n_{\rm H\,II} n_e \alpha_B(T)$ divided by ionization rate density $\Gamma^{ph}_{\rm H\,I} n_{\rm H\,I}$ versus baryon overdensity Δ_b, where

$$\Gamma^{ph}_{\rm H\,I} = \frac{cE}{h}\left[\int_{\nu_{\rm H\,I}}^{\infty} \frac{\sigma_{\rm H\,I}(\nu)\chi_E(\nu)}{\nu}\, d\nu\right] \Big/ \left[\int_{\nu_{\rm H\,I}}^{\infty} \chi_E(\nu)\, d\nu\right]. \quad (23)$$

Here, $\sigma_{\rm H\,I}(\nu)$ and $\nu_{\rm H\,I}$ are the ionization cross section and ionization threshold for H I, respectively, and h is Planck's constant (Paper I). In the middle column, we plot the relative bin contribution to the total recombination rate density versus Δ_b. We draw vertical lines at $\Delta_b = 1$ and 100, and in the legend box calculate the cumulative contribution to total reionizations to those thresholds. In the right column, we plot the cell recombination time divided by the Hubble time versus Δ_b. All three columns evolve with decreasing redshift from top to bottom.

At $z \sim 9$, in the left column of Figure 11, we see that even though there are regions of the volume that are in approximate ionization equilibrium (indicated by the horizontal distribution near 10^0), there is a wide distribution of cells far out of equilibrium. The middle column shows that about 37% of all recombinations happen below a Δ_b of 100, and about 3.2% happen below Δ_b of 1. The phase diagram in the right column shows that there is a bimodal distribution of cells in terms of their recombination time normalized by Hubble time. The top concentration of cells are more neutral, having long recombination times, and the lower concentration of cells are photoionized, having smaller recombination times. The recombination time is lower for the ionized cells simply because there are more free electrons available to recombine with protons. The blue cloud at low Δ_b and high $t_{\rm rec}/t_{\rm Hubble}$ represents the small number of cells that are shock heated to $T > 10^6$ K by supernova feedback. Due to this high temperature, even though there are more free electrons, their recombination times remain long.

At $z \sim 7$, more of the volume has reached the Well Ionized level, and we see the size of the out of equilibrium distribution shrink in the left column. The middle column shows about 40% of total recombinations are happening below Δ_b of 100, and about 4.2% happens below Δ_b of 1. In the right column, we see roughly equal numbers of cells in the upper (more neutral) distribution as compared to the lower (more ionized) distribution, whereas the top was much greater in numbers before. As more cells become ionized to a high degree, their recombination time will decrease and their cell counts will shift to the lower distribution.

At $z \sim 6$, looking at the left column, most of the cells are now in equilibrium and the spread in the distribution out of equilibrium continues to narrow. This is indicated by the peak of the distribution in red, being near zero on the y-axis. The middle column shows 30% and 3.8% recombinations below Δ_b of 100 and 1, respectively. The right column shows that the majority of the cells are now in the more ionized distribution and have a low recombination time. This can be verified by looking at the same redshift in Figure 7, where most of the cells are at the Well Ionized level compared to fewer before.

At $z \sim 5.5$, after the entire volume has become Well Ionized, and the vertical spread of the distribution has collapsed to about an order of magnitude away from equilibrium with the vast majority of the cells in equilibrium. The fraction of recombinations are 25% and 4% below Δ_b of 100 and 1, respectively. Looking at the recombination time to Hubble time, we no longer see the bimodal distribution of neutral cells and highly ionized cells, we only see the bottom distribution of highly ionized cells now. The small distribution of shock heated gas is still present, but now seem more prominent with the absence of the neutral distribution.

At $z \sim 5$, in the left column, the few cells that are in the low density void, which were recombining slower than ionizing are now all near equilibrium. Cells that are higher in Δ_b are more likely to be above equilibrium. In the middle column, we see the fraction of recombinations are 16% and 2.9% for region below Δ_b of 100 and 1, respectively. Not much has changed in the recombination time column except there are fewer cells above the Δ_b of 10^4, possibly due to effect of Jeans smoothing.

We see that there is no real one-to-one correspondence between overdensity and the quantities we show on the y-axis. That is because in a given panel we are only seeing two dimensions of a multidimensional physical process that depends on locality to sources of radiation, the behavior of said sources at a given moment, the local density of neutral and ionized gas, temperature, among others. It is helpful to discuss the average behavior in any given overdensity as we have done, but we should always keep in mind that the average may not be as representative of the wider distribution as we may believe.

4.3. Investigating Thresholded Clumping Factor Analyses

4.3.1. Excluding Halos

We saw in Section 4.1 that using the unthresholded H II density field to calculate C via Equation (16) yields a reasonably good estimate of when reionization completes (Figure 8). This is perhaps not surprising since we count every ionizing photon emitted and every recombination to the accuracy of Equation (22). Possible sources of disagreement between theory and simulation are (1) inaccuracies in estimating the recombination rate density using Equation (22), (2) breakdown of the "instantaneous approximation" used to derive Equation (22) due to history-dependent effects, (3) finite propagation time for I fronts to cross voids, and (4) numerical inaccuracies. Regarding possibility (4), we note that our mathematical formalism is photon conserving, and that our I-front tests in Paper I show that I fronts propagate at the correct speed, which is an indication that numerical photon conservation is good.

To investigate whether improved estimates of the recombination rate density will improve the agreement, we follow the practice of some recent investigators (Pawlik et al. 2009; Raicevic & Theuns 2011) and threshold out dense gas bound to halos, leaving only the diffuse IGM to consider. The motivation for this is that since we are only interested in the photon budget required to maintain the diffuse IGM in an ionized state, by excluding the complicated astrophysics within halos we have a simpler problem to model and resolve numerically.

To proceed, we must calculate the ionization and recombination rate densities outside of collapsed objects. We estimate

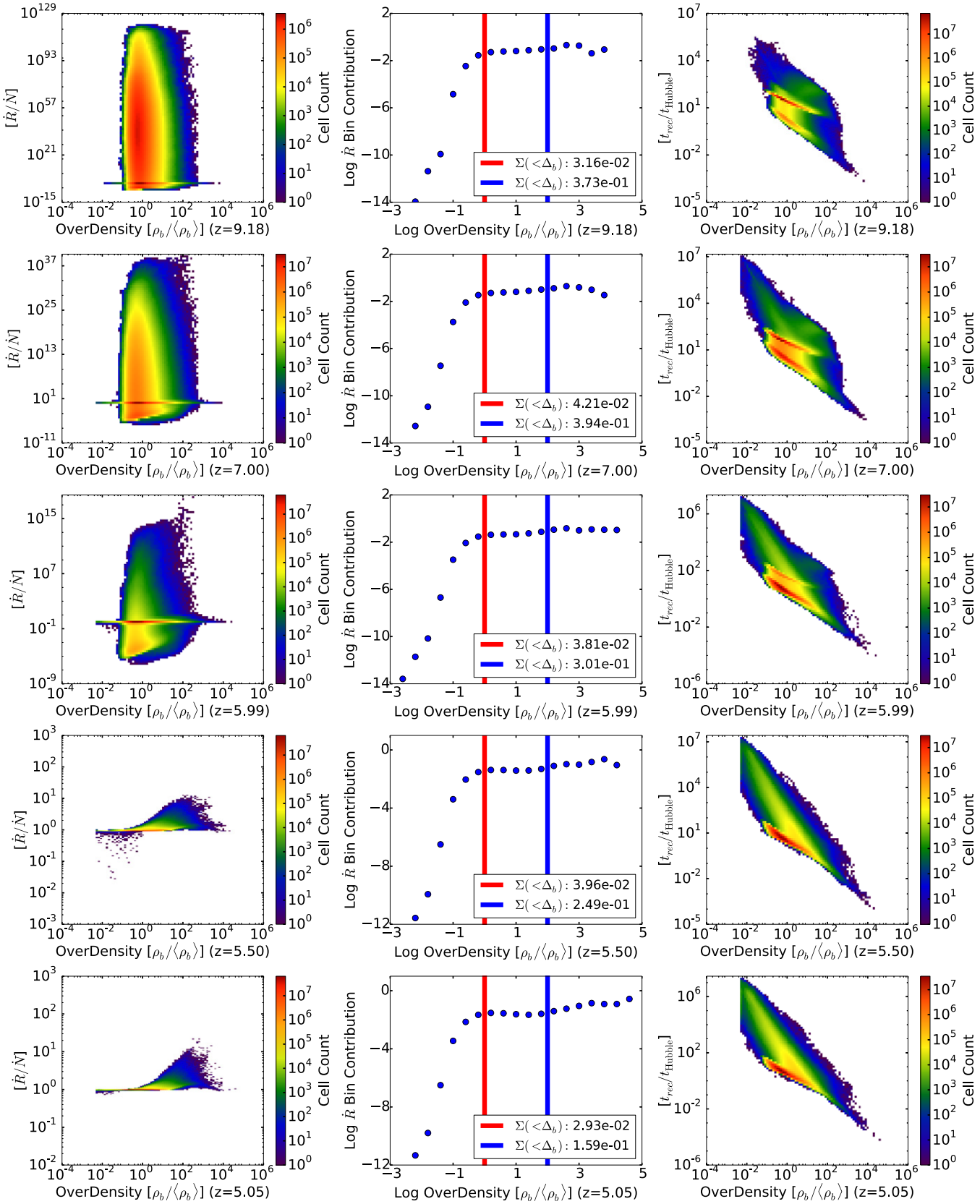

Figure 11. Quantifying recombination information. The left column is a 2D distribution of recombination rate density divided by ionization rate density vs. overdensity. The middle column is plot relative bin contribution to the total recombination rate density vs. overdensity bins. The lines show the cumulative of all previous bins. The blue line is at $\Delta_b = 100$ and the red line is at $\Delta_b = 1$. The right column is plot of recombination time divide by Hubble time vs. overdensity. All three columns evolve with decreasing redshift from top to bottom.

(A color version of this figure is available in the online journal.)

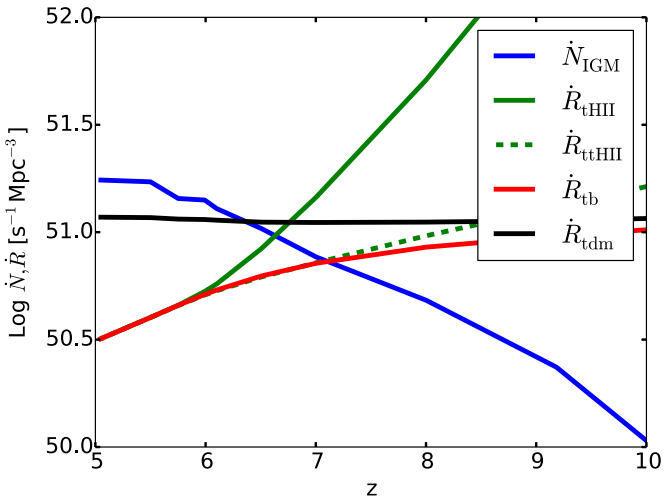

Figure 12. Same quantities as Figure 8, except now the "$\dot{N}_{\rm IGM}$" curve is the number of ionizing photons that escape into the IGM (see Section 5). The recombination rate densities with a subscript that begins with "t" are calculated as described in the caption for Figure 8, except that the clumping factors are computed excluding regions satisfying $\Delta_b > 100$. The curve labeled $\dot{R}_{\rm ttH\,II}$ is calculated from Equation (22) using the doubly thresholded clumping factor $C_{\rm ttH\,II}$ defined in Figure 13.

(A color version of this figure is available in the online journal.)

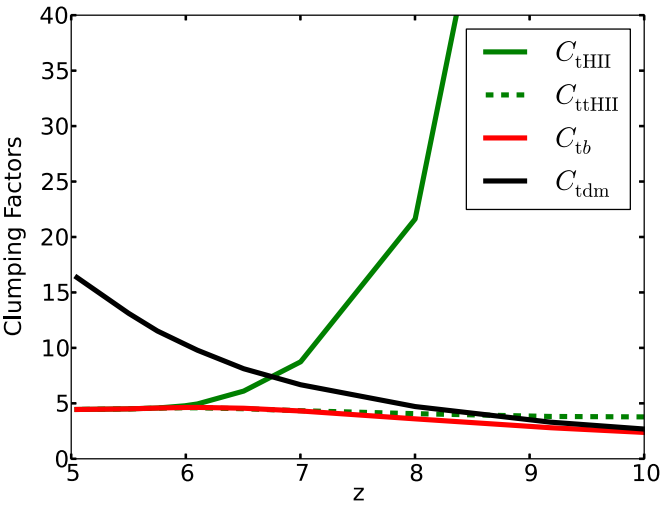

Figure 13. Thresholded clumping factors used in Figure 12. $C_{\rm tH\,II}$, C_{tb}, $C_{\rm tdm}$ are calculated using thresholded H II, baryon, and dark matter density fields, respectively, where only cells satisfying $\Delta_b < 100$ contribute. $C_{\rm ttH\,II}$ is calculated from the H II density, where only cells satisfying $\Delta_b < 100$ and $f_i > 0.1$ contribute.

(A color version of this figure is available in the online journal.)

the number of ionizing photons escaping halos by multiplying $\dot{N}_{\rm sim}(z)$ by a global escape fraction $\bar{f}_{\rm esc}(z)$ derived in Section 5 and plotted in Figure 21:

$$\dot{N}_{\rm IGM}(z) = \bar{f}_{\rm esc}(z)\dot{N}_{\rm sim}(z). \quad (24)$$

The recombination rate density outside of halos is calculated using Equation (22), where now the clumping factor is thresholded such that only cells for which $\Delta_b < 100$ contribute to the sum. As in Figure 8, we plot three curves for the recombination rate density calculated using Equation (22) using H II, baryons, and dark matter density fields. These are plotted in Figure 12 as green, red, and black curves, respectively. The corresponding clumping factors are plotted in Figure 13. We see

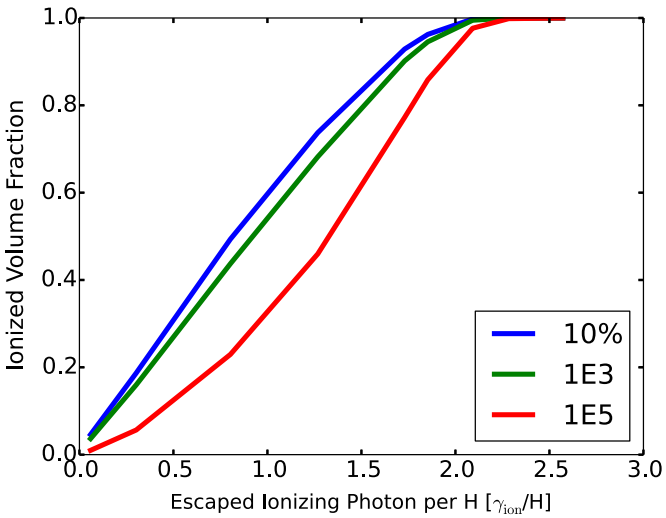

Figure 14. Ionized volume fraction as a function of the number of ionizing photons emitted per H atom averaged over the entire simulation volume (excluding gas inside halos) for three different ionization levels: $f_i \geqslant 0.1$ (blue line); $f_i \geqslant 0.999$ (green line); $f_i \geqslant 0.99999$ (red line). Compare with Figure 10, which includes gas inside halos.

(A color version of this figure is available in the online journal.)

that the recombination rate density based on the singly thresholded H II (labeled $\dot{R}_{\rm tH\,II}$) and on the thresholded dark matter (labeled $\dot{R}_{\rm tdm}$) curve cross the ionizing emissivity curve labeled "$\dot{N}_{\rm IGM}$" at $z \approx 6.7$ in Figure 12, whereas the thresholded baryon density curve (labeled $\dot{R}_{tb}$) crosses "$\dot{N}_{\rm IGM}$" at $z \sim 7.2$. Taking the doubly thresholded H II curve as the best estimate for the recombination rate density, we find that restricting the analysis to only IGM gas yields poorer agreement than the simpler, global model of Madau, which at first blush is a perplexing result. By thresholding out the gas in galaxies, we have isolated about the subject in which we are interested: the ionization balance of the IGM. Why then should the implied redshift of reionization completion become worse compared to the analysis in Section 4.1? We defer addressing this question until later sections.

Finally, we ask how many ionizing photons per H atom are required to convert the neutral gas residing outside halos to a well ionized state. We repeat the analysis of Figure 10 and show the result in Figure 14. We see that the effect of counting only escaped photons on the photon budget is significant. Previously, we summed $\dot{N}_{\rm sim}(z)$ and divided by the total number of hydrogen atoms in the simulation volume, and used that as our progress variable. In Figure 14, we sum $\dot{N}_{\rm IGM}(z)$ and divide by the number of hydrogen atoms in the thresholded volume and use that as our progress variable. Instead of needing ~four to ionize the IGM, now we only need ~two photons per hydrogen atom for 99.9% of the universe to reach the Well Ionized level. This number should not be confused with the quantity discussed by Bolton & Haehnelt (2007), Becker & Bolton (2013) in connection with the so-called photon-starved reionization scenario. The latter is the ratio of the instantaneous ionizing emissivity per gigayear per hydrogen atom, measured considerably after reionization is completed. We discuss this topic further in Section 7.2.

4.3.2. Including Temperature Corrections

During the preparation of this paper, a new way of estimating the recombinations in the IGM appeared in the literature. The authors (Shull et al. 2012; Finlator et al. 2012) reformulated the expression for the clumping factor taking the temperature

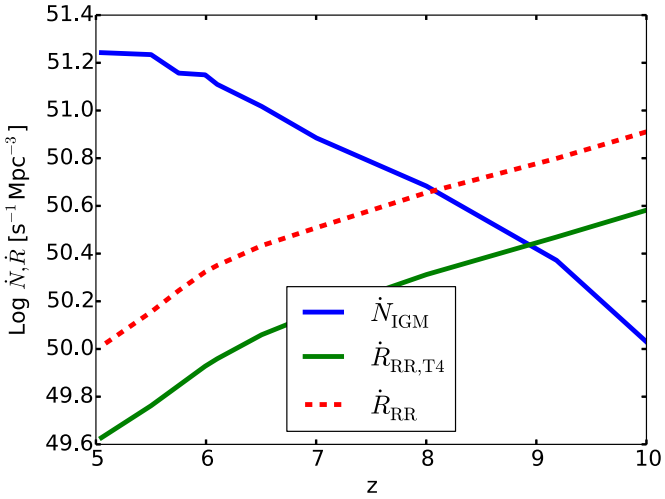

Figure 15. Ionizing photon injection rate density in the IGM from the simulation $\dot{N}_{\rm IGM}$ vs. the predictions of Equation (26), evaluated with two choices for the clumping factor which take temperature corrections into account. The curve labeled "$\dot{R}_{\rm RR,T4}$" is from Equation (26), with T_4 being the average temperature in $C_{\rm RR}$ region in units of 10^4 K. The curve "$\dot{R}_{\rm RR}$" is calculated the same way as $\dot{R}_{\rm RR,T4}$ except now T_4 is set to 1 in Equation (26), for an effective IGM temperature of 10^4 K.

(A color version of this figure is available in the online journal.)

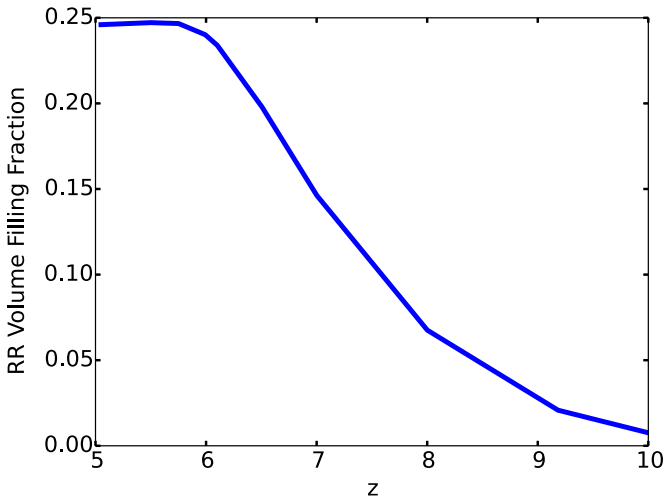

Figure 16. Evolution of the volume filling fraction with redshift of regions satisfying the $C_{\rm RR}$ thresholding criteria.

(A color version of this figure is available in the online journal.)

dependence of the recombination rate into account. We briefly investigate their methods here. In order for the calculation of the clumping factor to take only IGM gas that is ionized but recombining, several additional thresholds were applied. Equation (15) in Shull et al. (2012) is a new expression for the clumping factor, similar in form to Gnedin (2000a),

$$C_{\rm RR} = \frac{\langle n_e n_{\rm H\,II} \alpha_B(T) \rangle}{\langle n_e \rangle \langle n_{\rm H\,II} \rangle \langle \alpha_B(T) \rangle} \quad (25)$$

with the following thresholds applied: $1 < \Delta_b < 100$, 300 K $< T < 10^5$ K, $Z < 10^{-6}\ Z_\odot$, $x_e > 0.05$. Here, Z is metallicity and x_e is the ionized fraction. The reason that a lower limit threshold is applied to the baryon overdensity, the authors argued, is because very little recombinations happen there, due to the low density. Shull et al. (2012) also provide a new formulation for ionizing photon rate density that uses this definition of the clumping factor, in their Equation (10),

$$\frac{dN}{dt} = 4.6 \times 10^{50}\ {\rm s}^{-1}\ {\rm Mpc}^{-3} \times \left(\frac{(1+z)}{8}\right)^3 T_4^{-0.845} \left(\frac{C}{3}\right). \quad (26)$$

Here, T_4 is the mean IGM temperature measured in units of 10^4 K.

Equation (26) is proposed as an improvement over Equation (1). To see if this is the case, we used our data to evaluate the clumping factor $C_{\rm RR}$ and then used Equation (26) to calculate ionizing photon rate density versus redshift needed to maintain an ionized IGM. The result is shown in Figure 15. The curve labeled $\dot{R}_{\rm RR,T4}$ in green uses the average temperature, in units of 10^4 K, of the region that satisfies the $C_{\rm RR}$ thresholds for T_4 in Equation (26). The curve $\dot{R}_{\rm RR}$ uses 1 in place of T_4 in Equation (26), essentially fixing the IGM temperature to a constant 10^4 K. The green curve is lower than the red curve because the average temperature in the simulation is higher than 10^4 K. The blue curve labeled $\dot{N}_{\rm IGM}$ is as defined previously. We see that Equation (26) predicts that reionization completes at significantly higher redshifts than exhibited by the simulation, calling into question the validity of the analysis.

We find it curious that as the clumping factor analysis is refined through physically well-motivated modifications, it yields predictions for the redshift of reionization completion that become increasingly worse, moving to higher redshift rather than lower redshift. This suggests that there is something fundamentally wrong with the whole approach, and that the seemingly good agreement found in Section 4.1 was fortuitous. One worrisome aspect about the utility of Equation (26) is that the fraction of the simulation volume included in the $C_{\rm RR}$ thresholds is actually quite small. This is illustrated in Figure 16. The included volume grows from 3% at $z = 9$ to only 23% of the simulation volume by overlap. One wonders about the validity of making global statements about reionization based on such a restricted sample of the IGM. It is also unclear how we should interpret the redshift at which lines across in Figure 15. Should we interpret it as the redshift below which an ionization rate given by Equation (26) can keep the whole volume ionized, or only the fraction of the volume satisfying the thresholds? If it is the former, how do we account for the time it takes for I fronts to cross neutral voids?

At this point, the reader may rightfully claim that the Madau-type analysis was never meant to predict the precise redshift for reionization completion, only the ionization rate density needed to maintain the IGM in an ionized state after reionization has completed. We would agree with that. However, it is effectively being used in this way when it is applied to galaxy populations at increasingly higher redshifts $z = 6$–7 (see Fan et al. 2006; Robertson et al. 2013). Our investigations indicate that formulae such as Equation (1) and (26) are not reliable estimates of when reionization completes. In Section 7, we examine whether they can be usefully applied at lower redshifts, as originally intended.

4.4. Comparing Clumping Factors

For ease of comparison, we collect all of the H II clumping factors used in the previous sections into one plot. The unthresholded H II calculated using Equation (16) is denoted $C_{\rm H\,II}$. The singly thresholded clumping factor is denoted $C_{\rm tH\,II}$, in which the threshold $\Delta_b < 100$ is being applied. The curve labeled $C_{\rm RR}$

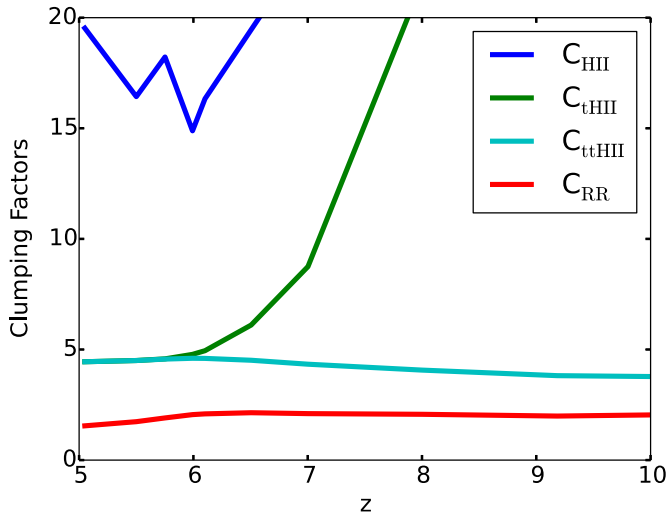

Figure 17. Various clumping factors vs. redshift. $C_{\rm H\,II}$ is Equation (16) used in $\dot{R}_{\rm H\,II}$ curve in Figure 8, $C_{\rm tH\,II}$ is used in $\dot{R}_{\rm tH\,II}$ curve in Figure 12, $C_{\rm ttH\,II}$ is clumping factor with two thresholds applied, $\Delta_b < 100$ and $X_e > 0.05$, shown here solely for comparison. $C_{\rm RR}$ is the value of recombination rate clumping factor from Equation (25) with the five thresholds applied.

(A color version of this figure is available in the online journal.)

plots the evolution of Equation (25) with the following thresholds: $1 < \Delta_b < 100$, 300 K $< T < 10^5$ K, $x_e > 0.05$. For comparison, we also plot a doubly thresholded H II clumping factor denoted $C_{\rm ttH\,II}$ with thresholds $\Delta_b < 100$ and $x_e > 0.05$, which can be thought of as the clumping factor inside H II regions excluding the dense gas in halos.

We see a clear trend that as more thresholds are applied the lower the value of the clumping factor goes. This is because as more regions of the volume are excluded from the averaging process the remaining regions are more homogeneous exhibiting less variations. If no thresholds are applied, the H II clumping factor starts around 200 at $z \sim 9$ (Figure 8). Such high values arise because when the first couple of ionizing sources created high H II, they are localized and spread far apart, making the H II density very clumpy. As more of the universe is ionized, the H II density becomes more homogeneous. We see the single and double thresholded H II clumping factors become the same after overlap with a value of ∼4.5 because the second threshold $x_e > 0.05$ is satisfied everywhere.

The clumping factor that is not based on the H II density alone is $C_{\rm RR}$. We see from Equation (25) that $C_{\rm RR}$ depends on electron number density, H II number density, and the case B hydrogen recombinationation coefficient $\alpha_B(T)$, which is itself dependent on the gas temperature T (fit to Table 2.7 in Osterbrock & Ferland 2006 implemented in *Enzo*). $\alpha_B(T)$ depends on T to a negative power and this causes Equation (25) to sometimes have a very low numerator compared to the denominator. This as well as the exclusion of gas in the voids leads to the low clumping factor value of ∼two we see in the graph. It is very possible to have a value that is smaller than unity, which can lead to even more confusion with the original definition of the clumping factor in Equation (16). There, the clumping factor can only have a value of greater than one, and one occurs only in the case of homogeneous distribution of the gas number density.

5. A GLOBAL ESTIMATE FOR CIRCUMGALACTIC ABSORPTION OF IONIZING RADIATION

The ionizing escape fraction from galaxies is an important parameter in models of reionization. Typically, one thinks about the escape fraction as a property of individual galaxies, determined by the absorption of ionizing radiation on small scales in the interstellar medium (ISM). However it is interesting to ask whether there is significant absorption in the denser circumgalactic medium (CGM) surrounding galaxies. If we write the total escape fraction as the product of escape fractions, then $f_{\rm esc} = f_{\rm esc}({\rm ISM})\, f_{\rm esc}({\rm CGM})$. Here we use our simulation to derive an estimate of the globally averaged escape fraction as a function of redshift due to the circumgalactic medium $\bar{f}_{\rm esc}({\rm CGM})$.

Recall from Section 2 that the halo escape fraction is not a model input parameter, but is rather an output since the equation of radiative transfer is solved throughout the computational domain. Our halos are not well resolved internally, and so we are underestimating the amount absorption of ionizing radiation on galaxy ISM scales. However, if significant absorption occurs on scales of the virial radius or larger, then that would be simulated reasonably accurately. In the following, we assume that this is the case, and present results that can be taken to be an upper limit on the total escape fraction (ISM+CGM).

Rather than measure the escape fraction halo by halo and take the average over all halos, we use a simpler method. Since we know every ionization requires an ionizing photon, and we have the ionization rate density as a field defined at every grid cell, then we can estimate $\bar{f}_{\rm esc}({\rm CGM})$ as follows (hereafter we drop the CGM modifier with the reader's understanding that this is what we are estimating):

$$\bar{f}_{\rm esc}(I_t) = \int_{V_t} n_{\rm H\,I}\Gamma^{ph}_{\rm H\,I} d^3x \Big/ \int_V n_{\rm H\,I}\Gamma^{ph}_{\rm H\,I} d^3x, \qquad (27)$$

where $\Gamma^{ph}_{\rm H\,I}$ is evaluated cell by cell via Equation (23), V is the simulation volume, and V_t denotes the integration includes only cells which satisfy $\Delta_b < 100$. In other words, $\bar{f}_{\rm esc}$ is the ratio of the number of ionizations in the IGM, as defined by the overdensity threshold, to the total number of ionizations in the volume. The modifier I_t refers to this method of estimating $\bar{f}_{\rm esc}$ (a superior method is presented below).

The result is plotted in Figure 18. At high redshifts the escape fraction is high and relatively constant at $\bar{f}_{\rm esc} \sim 0.65$–$0.7$. As overlap is approached $\bar{f}_{\rm esc}$ drops considerably, reaching values of ∼0.2 by $z = 5$. There is no obvious reason why the escape fraction should drop so dramatically at the epoch of overlap. To investigate this properly would require a statistical analysis of individual halo escape fractions, which we defer to a subsequent paper. Perhaps this is an artifact of how we are estimating $\bar{f}_{\rm esc}$. While it is true that every ionization requires and ionizing photon, after overlap the volume becomes optically thin to ionizing radiation, and it is not true that every ionizing photon causes an ionization in the box. This is illustrated in Figure 19.

The curve labeled $\dot{N}_t$ is the actual ionization rate density measured in the simulation averaged over the entire 20 Mpc cubic volume satisfying the overdensity threshold $\Delta_b < 100$; i.e., precisely the numerator of Equation (27) divided by 20^3. The curve labeled $\dot{R}_t$ is the recombination rate density averaged over the same volume; i.e.,

$$\dot{R}_t = \int_{V_t} n_e n_{\rm H\,II} \alpha_B(T) d^3x. \qquad (28)$$

We see that ionization rate density $\dot{N}_t$ grows with redshift and reaches a maximum at $z \approx 6.5$, and then drops by roughly 0.8 dex by overlap completion at $z = 5.8$. It continues to

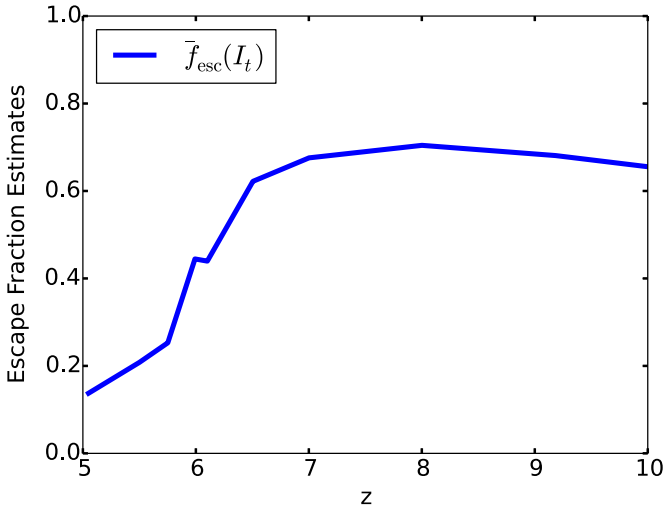

Figure 18. Estimate of the globally averaged ionizing radiation escape fraction due to circumgalactic absorption $\bar{f}_{\rm esc}(I_t)$ computed as the ratio of the volume-integrated ionization rate in the IGM ($\Delta_b < 100$) divided by the total ionization rate (Equation (27)).

(A color version of this figure is available in the online journal.)

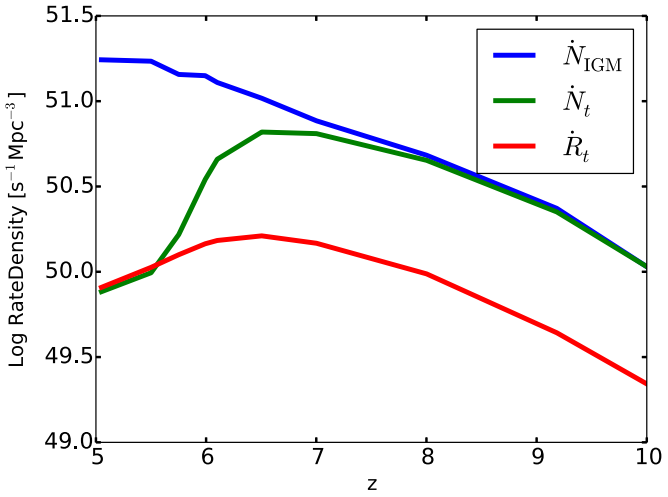

Figure 19. Evolution of the volume-averaged rate densities for (1) ionizing photons injected into the IGM ($\dot{N}_{\rm IGM}$), (2) gas photoionization ($\dot{N}_t$), and (3) gas recombination ($\dot{R}_t$) integrated over the singly thresholded volume V_t defined as $\Delta_b < 100$. The ionization rate density curve tracks the photon injection rate density curve at high redshifts, but begins to fall below it as the globally averaged ionization parameter approaches unity (Figure 20). After overlap, in the photon abundant regime, the ionization rate density is $\sim$20$\times$ the photon injection rate density, but comes into balance with the recombination rate density.

(A color version of this figure is available in the online journal.)

decrease thereafter. The reason for this sudden drop is that after overlap there are very few neutral atoms left to ionize ($n_{\rm H\,I}/n_{\rm H} \sim 10^{-5}$).

This can be illustrated by considering the global ionization parameter, which is the number of ionizing photons per neutral H atom $\Gamma_{\rm IP} = \langle n_{ph}\rangle/\langle n_{\rm H\,I}\rangle$ averaged over the entire volume. Specifically, we integrate the gray radiation energy density divided by the mean photon energy $\bar{\epsilon}$ over the singly thresholded volume, and divide by the number of H I atoms in the same volume:

$$\Gamma_{\rm IP} = \int_{V_t} (E/\bar{\epsilon}) d^3x \Big/ \int_{V_t} n_{\rm H\,I} d^3x. \quad (29)$$

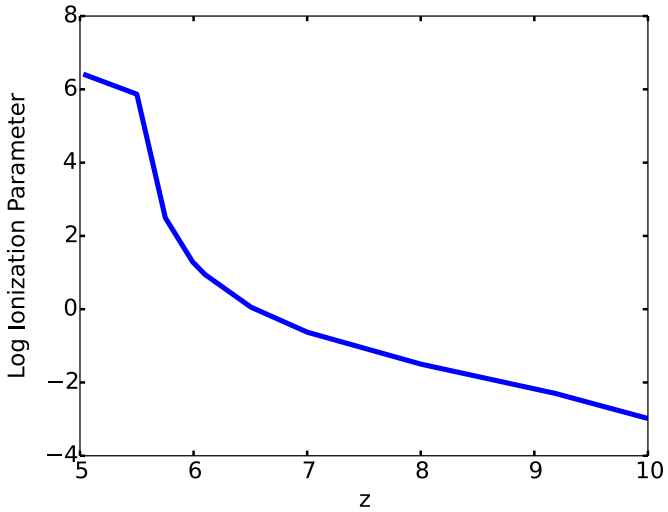

Figure 20. Redshift evolution of the global H I ionization parameter as defined in Equation (29).

(A color version of this figure is available in the online journal.)

We see from Figure 20 that $\Gamma_{\rm IP}$ grows from $\sim 10^{-3}$ at $z = 10$ to unity at $z \approx 6.5$ just before overlap. Thereafter $\Gamma_{\rm IP}$ grows very rapidly, reaching a value around 10^5 at the overlap redshift, and leveling off at around 10^6 below that.

Returning to Figure 19, we see that the recombination rate density $\dot{R}_t$ curve tracks the ionization rate density curve to $z \sim 7$, but is about 0.7 dex lower in magnitude, as it must be if the ionized volume filling fraction is to grow. As overlap is approached, ionizations and recombinations come into balance, but the recombination rate density has dropped considerably since it reached its maximum value at $z \approx 6.5$. This is also the redshift at which the ionization rate achieves a maximum, and when the global ionization parameter reaches unity. We also observe that the $f_{\rm esc}$ curve in Figure 18 begins its precipitous drop at this redshift. We believe all of these events signal the rapid rise in the global ionization parameter below $z = 6.5$, and not some change in the escape fraction of young galaxies.

Counting the fraction of all ionizations occurring outside halos is not a reliable estimate of the escape fraction for $\Gamma_{\rm IP} \gg 1$ because it does not count the photons in the radiation field that have nothing to ionize. Therefore we need to modify Equation (27) to include photons that build up the radiation field:

$$\bar{f}_{\rm esc} = \int_{V_t} \left(n_{\rm H\,I}\Gamma^{ph}_{\rm H\,I} + \frac{1}{\bar{\epsilon}}\frac{dE}{dt} \right) d^3x \Big/ \int_V (\eta/\bar{\epsilon}) d^3x. \quad (30)$$

Here the numerator is the rate at which ionizing photons are causing ionizations in the IGM and building up the UV background, and the denominator is volume-integrated ionizing photon production rate.

Figure 21 plots $\bar{f}_{\rm esc}$ calculated according to Equation (30). Each contribution to $\bar{f}_{\rm esc}$ is plotted separately, as well as the sum. We see that $\bar{f}_{\rm esc}$ is roughly constant with redshift with a value of around 0.6. We see that as the contribution due to ionizations declines below $z \sim 7$, the contribution due to the change in radiation background intensity increases in a compensating fashion. This confirms our earlier suspicions and gives us a better estimate of the mean circumgalactic attenuation of ionizing radiation from young galaxies.

To complete the picture, we plot in Figure 19 the number density of ionizing photons escaping into the IGM, calculated as

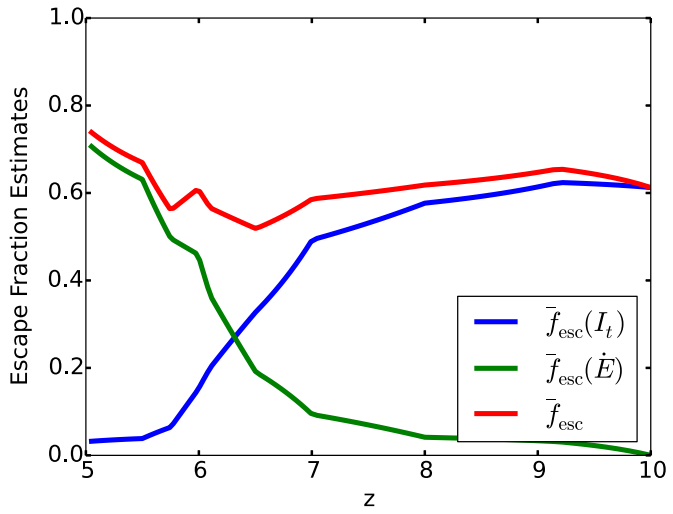

Figure 21. Redshift evolution of the globally averaged escape fraction contribution from circumgalactic absorption as estimated by the number of ionizations occurring in the IGM and the buildup of the ionizing radiation background. The curves labeled $\bar{f}_{\rm esc}(I_t)$, $\bar{f}_{\rm esc}(\dot{E})$ plot the contributions of the first and second terms in Equation (30), while the curve labeled $\bar{f}_{\rm esc}$ plots their sum.

(A color version of this figure is available in the online journal.)

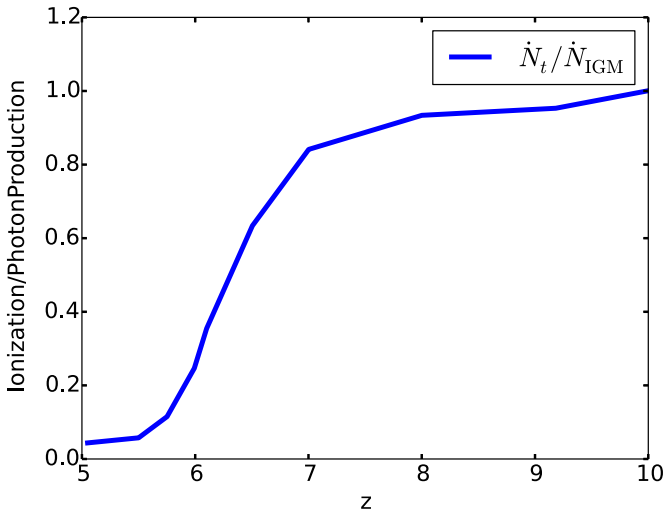

Figure 22. Ratio of the volume-integrated photoionization rate in the IGM $\dot{N}_t$ to the integrated photon injection rate into the IGM $\dot{N}_{\rm IGM}$, where the IGM is defined as cells with $\Delta_b < 100$. The ratio is near unity initially, remains high until $z \approx 7$ ($Q_{\rm H\,II} \approx 0.5$), and then drops rapidly as overlap is approached and the IGM becomes highly ionized.

(A color version of this figure is available in the online journal.)

$\dot{N}_{\rm IGM} = \bar{f}_{\rm esc}\dot{N}_{\rm sim}$, where $\dot{N}_{\rm sim}$ is the ionizing photon production rate in the simulation, and $\bar{f}_{\rm esc}$ is the improved estimate for the escape fraction calculated using Equation (30). We see that at high redshifts the $\dot{N}_{\rm IGM}$ and $\dot{N}_t$ track each other closely. This tells us two things. First, that reionization at high redshifts when $Q_{\rm H\,II} \ll 1$ is efficient, in the sense that every ionizing photon emitted results in an ionization. Second, that our estimate of $\bar{f}_{\rm esc}$ is reasonably accurate at these redshifts. However, as redshift decreases, the two curves systematically begin to deviate from one another in the sense that $\dot{N}_t < \dot{N}_{\rm IGM}$. Beginning at $z = 6.5$, the ionization rate density begins to decrease while the ionizing photon production rate into the IGM continues to rise. After overlap the large disparity between the $\dot{N}_{\rm IGM}$ and $\dot{N}_t$ curves can then be understood as indicating that the IGM becomes photon abundant.

The ratio of ionization rate density and the photon injection rate into the IGM is plotted in Figure 22. The ratio is unity initially, and slowly decreases until $z \approx 7$, and then drops rapidly as overlap is approached. After overlap the ratio is about 0.05. In other words, after overlap, the photon production rate is about 20 times the ionization rate in a volume-averaged sense. Since the ionization and recombination rates are in balance after overlap, we conclude that the volume averaged photon injection rate is about 20 times the recombination rate.

6. AN IMPROVED MODEL FOR THE EVOLUTION OF $Q_{\rm H\,II}$

In this section, we compare the evolution of the ionized volume fraction $Q_{\rm H\,II}$ from our simulation with the analytic model introduced by Madau et al. (1999). We are motivated to do this because, as we have seen from Section 4, Equation (1) is not a useful predictor of when $Q_{\rm H\,II}$ reaches unity. We therefore want to investigate the accuracy of the time-dependent model from which Equation (1) is derived as a limiting case.

Madau et al. (1999) derived the following ODE for the evolution of $Q_{\rm H\,II}$ (their Equation (20)):

$$\frac{dQ_{\rm H\,II}}{dt} = \frac{\dot{n}_{\rm ion}}{\bar{n}_{\rm H}} - \frac{Q_{\rm H\,II}}{\bar{t}_{\rm rec}}, \tag{31}$$

where $\dot{n}_{\rm ion}$ is the ionizing photon injection rate, $\bar{n}_{\rm H}$ is the mean density of H atoms in the universe, and $\bar{t}_{\rm rec}$ is some characteristic recombination time taking the clumpiness of the IGM into account. For a constant clumping factor and comoving emissivity, Madau et al. (1999) show that

$$Q_{\rm H\,II}(t) \approx \frac{\dot{n}_{\rm ion}}{\bar{n}_{\rm H}}\bar{t}_{\rm rec}. \tag{32}$$

Setting $Q = 1$, one arrives at $\dot{n}_{\rm ion}\bar{t}_{\rm rec} = \bar{n}_{\rm H}$, the basis for deriving Equation (1). Madau et al. (1999) state that this relation should still be valid provided the clumping factor and comoving emissivity are slowly varying on a timescale of $\bar{t}_{\rm rec}$. We utilize the differential form for our comparison because our emissivity is not a constant value, nor is it slowly varying on a recombination time as $Q \to 1$, as we show below.

A practical issue when testing Equation (31) is how $\bar{t}_{\rm rec}$ should be evaluated when $Q < 1$, and in particular when $Q \ll 1$. In the limit $Q \ll 1$, one is dealing with isolated H II regions evolving under the influence of local conditions. Yet the definition for $\bar{t}_{\rm rec}$ in Equation (21) invokes global values for C and $\langle n_{\rm H\,II}\rangle$. Should these quantitles be evaluated locally only within ionized regions? Or are global estimates good enough? In particular, since Madau et al. (1999)'s Equation (20) uses $\bar{n}_{\rm H}$ as a proxy for $\langle n_{\rm H\,II}\rangle$, what is the appropriate value for C to use?

A second practical issue is what to take for $\dot{n}_{\rm ion}$. This is commonly understood to be the rate at which ionizing photons are injected into the IGM (e.g., Haardt & Madau 2012, Section 9.3), which in our parlance is $\dot{N}_{\rm IGM}$. Or should we take the actual ionization rate density measured in the simulation $\dot{N}_t$? As we saw in the previous section, these two rates diverge as overlap is approached, and differ by more than an order of magnitude after overlap (Figure 22).

To examine these issues, we plot in Figure 23 $Q(z)$ from our simulation, as well as theoretical curves obtained by integrating Equation (31) under various assumptions. The curve labeled Q(sim) is the ionized volume fraction from our simulation that is at least 99.9% ionized (Well Ionized). The other four curves are obtained by integrating Equation (31) setting $\dot{n}_{\rm ion} = \dot{N}_t$ for

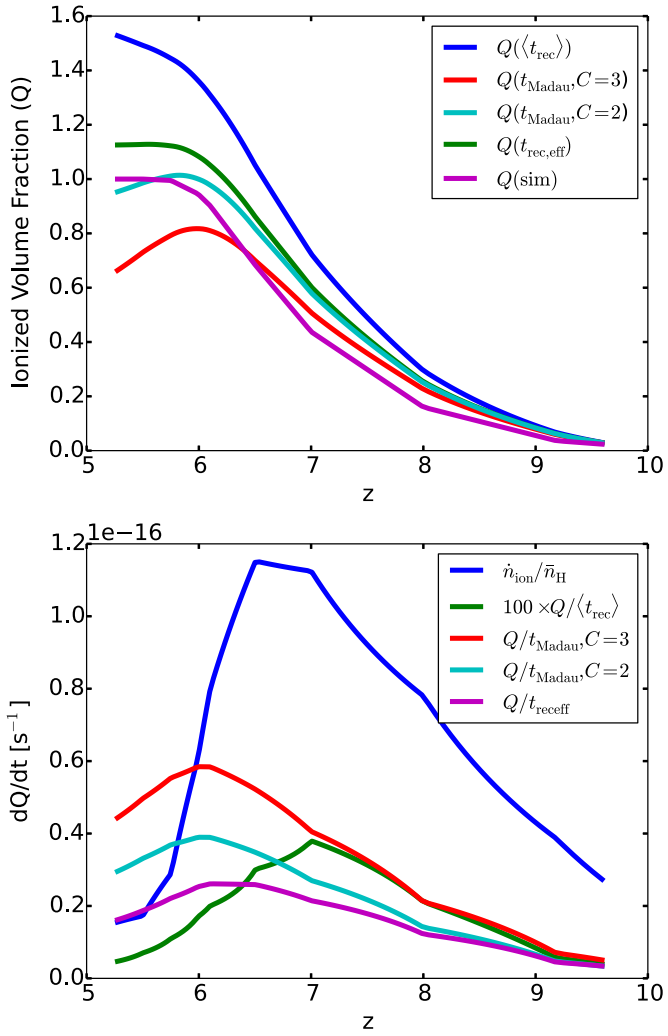

Figure 23. Top: comparison of the evolution of the ionized volume fraction Q from our simulation with the analytic model introduced by Madau et al. (1999). Q(sim) is calculated directly from counting the cells satisfying the Well Ionized threshold of $f_i > 0.999$. The other curves are calculated from integrating Equation (33) with the different expressions for $\bar{t}_{\rm rec}$ in Term$_2$, as described in the text. Bottom: plot of Term$_1$ and Term$_2$ individually using the different expressions for $\bar{t}_{\rm rec}$.

(A color version of this figure is available in the online journal.)

various choices for $\bar{t}_{\rm rec}$ (we investigate the $\dot{n}_{\rm ion} = \dot{N}_{\rm IGM}$ case at the end of this section.) The integral is approximated by summing a piecewise linear interpolation of the two terms on the RHS of Equation (31) using the trapezoidal rule:

$$Q(t) = \int_{t*}^{t} \frac{dQ}{dt} dt \approx \sum \frac{dQ}{dt} \Delta t = \sum_i (\text{Term}_1 - \text{Term}_2)_i \Delta t_i, \quad (33)$$

where $t*$ is the time when the first star forms in the simulation.

The curve labeled $Q(\langle t_{\rm rec}\rangle)$ uses the volume-averaged recombination time (volume average of Equation (18)). The two curves labeled $Q(t_{\rm Madau})$ use Equation (21) to evaluate $\bar{t}_{\rm rec}$ for $C = 2$ and 3, substituting $\bar{n}_{\rm H}$ for $\langle n_{\rm H\,II}\rangle$ and assuming a constant $T = 10^4$ K for the IGM. The curve labeled $Q(t_{\rm rec,eff})$ uses the effective recombination time definition

$$\bar{t}_{\rm rec} = t_{\rm rec,eff} \equiv \frac{\langle n_{\rm H\,II}\rangle}{\langle n_{\rm H\,II} n_e \alpha_B(T)\rangle}. \quad (34)$$

This particular definition makes the last line of Equation (20) true trivially, with no assumption about the IGM temperature or ionization state of the hydrogen. It involves no ad hoc clumping factors, and represents the actual appropriately averaged recombination time in the simulation. All the above volume-averaged quantities have the threshold of $\Delta_b < 100$ applied, and thus exclude dense gas bound to halos. Several of the curves derived from integrating dQ/dt reach values above unity at the end of the overlapping phase. While it is physically impossible to have $Q > 1$, it is not mathematically forbidden, and so we show the complete curves because they give us some insight about the relative contribution of the recombination term (Term$_2$) as compared to the ionization term (Term$_1$).

The $Q(\langle t_{\rm rec}\rangle)$ curve ionizes the quickest, reaching $Q = 1$ at $z \sim 6.5$, which is substantially before the simulation which achieves it at $z \approx 5.8$. The reason for this, as we will analyze shortly, is that recombinations play essentially no role in this model. The $Q(t_{\rm rec,eff})$ curve has the same shape as the Q(sim), but is everywhere higher, and crosses $Q = 1$ at $z \sim 6.1$. Given that this integration uses the actual ionization rate density and effective recombination time in the simulation, this discrepancy demands an explanation. We address this below. Finally the $Q(t_{\rm Madau})$ curves do not match the shape of the Q(sim) curve, ionizing more quickly at early times, and exhibiting a maximum value for Q at $z \sim 6$.

To understand this behavior more fully, we plot in Figure 23 bottom the values for Term$_1$ and Term$_2$ in Equation (31). The blue curve is Term$_1$ of Equation (31). The other four curves plot Term$_2$ with their respective values for $\bar{t}_{\rm rec}$. The ionization curve dominates all the recombination curves at high redshifts, and reaches a maximum at $z \sim 6.5$. This is a partial reflection of the plateauing and subsequent decline of the SFRD shown in Figure 3. More fundamentally, it is a reflection of the rapid drop in the neutral fraction of the IGM as overlap is approached. The curve using the volume averaged recombination time $\langle t_{\rm rec}\rangle$ yields such low values compared to the others that we multiply it by 100 to make it more visible. Although this is not the relevant recombination time to use, since it weights low-density regions, it is effectively the limiting case $\bar{t}_{\rm rec} \to \infty$. We can therefore interpret the blue curve in Figure 23(a) as an integration of the ionization term only. It is significantly higher than the Q(sim) curve, suggesting that recombinations are important in the simulation at some level. The ionization term dominates the recombination term by factors of 6–10 in the $t_{\rm rec,eff}$ curve until just before overlap, and the two terms come into balance after overlap. The two $t_{\rm Madau}$ recombination curves are subdominant to the ionization term until $z \sim 6$, and at lower redshifts they become dominant. This explains the turnaround in the corresponding Q curves in Figure 23(a).

The differences in the magnitude of the recombination curves in Figure 23(b), especially at higher redshifts, is directly attributable to the magnitude of $\bar{t}_{\rm rec}$. For completeness, we plot $\bar{t}_{\rm rec}$ versus redshift in Figure 24, both unnormalized and normalized by $t_{\rm Hubble}$. In addition to the three curves for $t_{\rm rec,eff}$ and $t_{\rm Madau}$ for $C = 2, 3$, we also plot $t_{\rm Madau}$ for $C = C_{\rm ttH\,II}$ and $C = C_{\rm tdm}$. We see that all the curves with the exception of the Madau formula curve using the thresholded dark matter clumping factor exhibit an increasing recombination time with decreasing redshift, in line with our expectations. The latter curve shows the opposite trend, which is due to the fact that the dark matter clumping factor increases with decreasing redshift, even if it is thresholded to exclude halos (see Figure 12 bottom). Among the remaining curves, the $t_{\rm rec,eff}$ has the highest values,

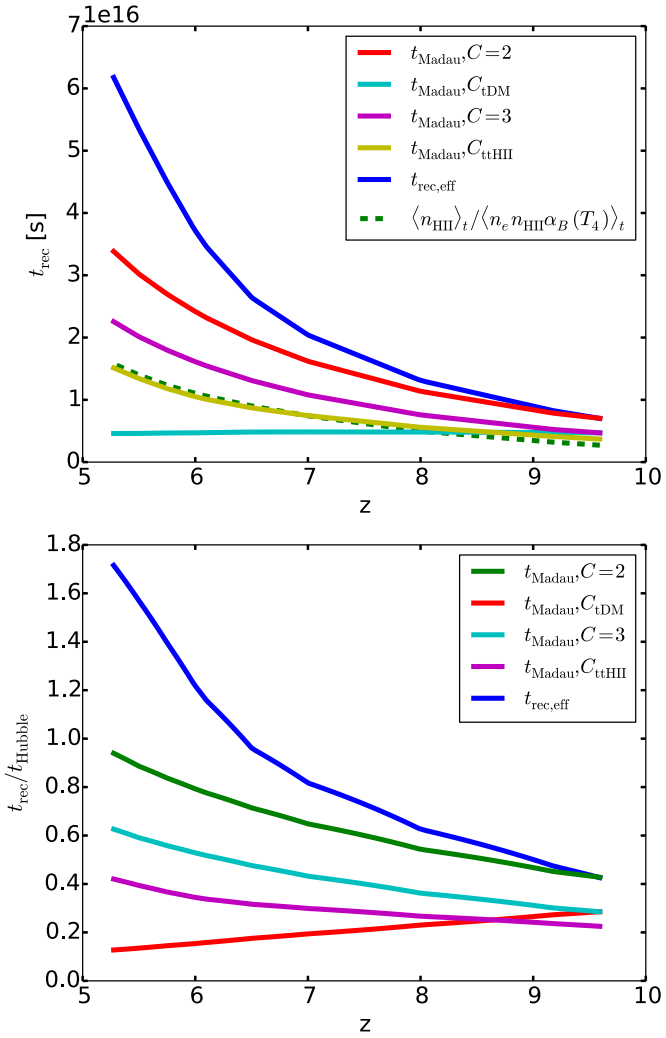

Figure 24. Top: recombination time vs. redshift, for various expressions for $\bar{t}_{\rm rec}$ as described in the text. The curve labeled $t_{\rm rec,eff}$ is the characteristic recombination time measured directly in the simulation. The curves labeled $t_{\rm Madau}$ evaluate Equation (21) for various choices for the clumping factor C. Bottom: recombination time vs. redshift normalized by the Hubble time, for various expressions for $\bar{t}_{\rm rec}$.

(A color version of this figure is available in the online journal.)

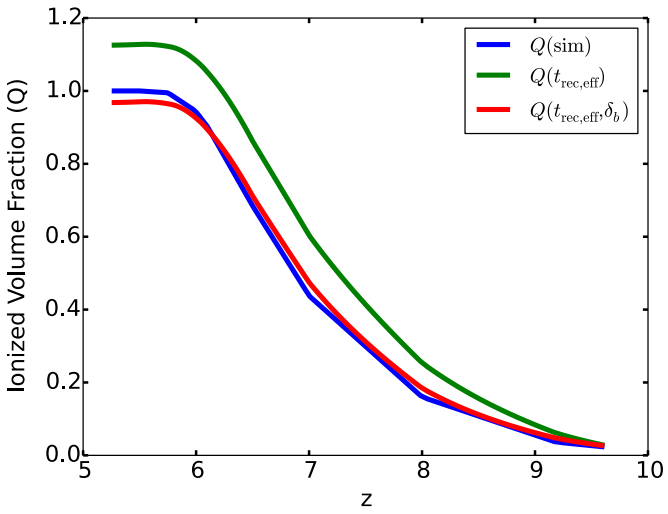

Figure 25. Improved agreement between theory and simulation. The green and blue curves are as in Figure 23. The red curve is obtained by integrating modified evolution equation for Q taking into account the overdensity effect of Inside-out reionization (Equation (35)).

(A color version of this figure is available in the online journal.)

and increases more sharply than the $t_{\rm Madau}$ curves due to the temperature of the IGM. To demonstrate that, we plot one additional curve (dashed curve) for $t_{\rm rec,eff}$ evaluated assuming a constant $T = 10^4$ K in the recombination rate coefficient.

We now comment on the often-made assumption in reionization models that $\bar{t}_{\rm rec} \ll t$. Madau et al. (1999) make this assumption in order to derive Equation (1). It is this assumption that allows for an instantaneous analysis of the photon budget to maintain the universe in an ionized state while ignoring history dependent effects. Referring to Figure 24(b) we see this is never true for $t_{\rm rec,eff}$ and it is not true for $t_{\rm Madau}$ at redshifts approaching overlap for any sensible value of C. We therefore conclude that history-dependent effects cannot be ignored, and that this is the reason Equations (1), (22), and (26) mis-predict the epoch of reionization completion. For the same reason, applying these formulae at lower redshifts is highly suspect.

Returning to the discrepancy between the Q(sim) and $Q(t_{\rm rec,eff})$ curves in Figure 23(a), since the most sensible choice for $t_{\rm rec}$ did not give us satisfactory agreement, we wondered what the origin of the discrepancy could be. Since we have shown that recombinations are relatively unimportant at high redshifts, but that the discrepancy is already present at high redshifts, the only possibility is that there is something wrong with the first term of Equation (33). When looking at the derivation for Equation (31) in Madau et al. (1999), it is stated that it "approximately holds for every isolated source of ionizing photon in the IGM." That got us thinking that our calculation of $\bar{n}_{\rm H}$ may be off from what is originally intended if it is a global average over the entire simulation box. Since the original dQ/dt is derived from the analytical Strömgren sphere model, it assumed a single ionizing source at the center of the volume, and the average density of the box is just the uniform density everywhere, we thought that might be the discrepancy. In an Inside-out model, I fronts are not initially propagating in a gas with an average density given by $\bar{n}_H$, but somewhat higher density. Would agreement improve if instead of using $\bar{n}_H$ in the first term of Equation (31), we used the local average density?

We therefore modify Equation (31) as follows:

$$\frac{dQ}{dt} = \frac{\dot{n}_{\rm ion}}{\delta_b \bar{n}_{\rm H}} - \frac{Q}{\bar{t}_{\rm rec}}, \tag{35}$$

where we have introduced in the denominator of the first term a factor $\delta_b \geqslant 1$, which corrects for the higher mean density within ionized bubbles. We measure δ_b from each redshift output as follows: $\delta_b = \langle \rho_b \rangle_{tt}/\langle \rho_b \rangle_t$. The volume average $\langle\rangle$ with subscript t is the usual $\Delta_b < 100$ threshold, the double subscript tt indicates the additional threshold of $x_e > 0.1$. Thus δ_b is the average baryon overdensity within Ionized regions excluding gas inside halos. Figure 26 shows a plot of δ_b versus Q together with a simple fitting formula which fits the data extremely well over the domain $0.01 \leqslant Q \leqslant 1$.

To see if this formulation improves agreement with our simulated data, in Figure 25 we integrate Equation (35) again setting $\dot{n}_{\rm ion} = \dot{N}_t$ and using $t_{\rm rec,eff}$ to evaluate the second term. For comparison, we show the curve obtained setting $\delta_b = 1$, which repeats a curve already presented in Figure 23. Although the simulated and integrated analytic model curves do not agree exactly, the $Q(\delta_b, t_{\rm rec,eff})$ curve shows much better agreement with the simulation, with error on the order of 1% instead of 10%.

By not assuming a constant emissivity and using the modified differential form in determining the volume filling fraction of Equation (35), we are able to more accurately model the evolution of the simulated volume filling fraction of H II to the Well Ionized level. For completeness, we plot in Figure 27 the evolution of $t_{\rm rec,eff}$ used in the above integration, including a reasonably good fit to the data.

Finally, we return to the question of what is the appropriate choice for $\dot{n}_{\rm ion}$ in Equation (35). This is commonly taken to be the rate at which ionizing photons are injected into the IGM (e.g., Haardt & Madau 2012, Section 9.3) because this can be connected to the observed UV luminosity density $\rho_{\rm UV}$ by the formula $\dot{n}_{\rm ion} = f_{\rm esc}\xi_{\rm ion}\rho_{\rm UV}$, where $f_{\rm esc}$ is the escape fraction for ionizing radiation, and $\xi_{\rm ion}$ is the rate of ionizing photons per unit UV (1500 Å) luminosity for the stellar population (Robertson et al. 2013). However, we have obtained excellent agreement between simulation and Equation (35) using the mean ionization rate density in the IGM $\dot{N}_t$, which differs from the ionizing photon injection rate density $\dot{N}_{\rm IGM}$ as $Q \rightarrow 1$. In Figure 28, we show the result of integrating Equations (31) and (35) with the choice $\dot{n}_{\rm ion} = \dot{N}_{\rm IGM}$, as originally proposed by (Madau et al. 1999). Also plotted in Figure 28 is Q(sim) (blue line) and our best agreeing model (green line). The red line ignores the δ_b correction, and deviates to the high side of Q(sim) almost immediately, for reasons we discussed earlier. It crosses $Q = 1$ at $z \approx 6.6$, which is too early by $\Delta z = 0.8$. The teal line includes the δ_b correction, and tracks the Q(sim) closely to $z \approx 7$, and thereafter deviates on the high side. It crosses $Q = 1$ at $z \approx 6.4$, which is too early by $\Delta z = 0.6$. Both curves show an accelerated change in Q as z decreases, which is characteristic of standard analytic ionization models (e.g., Haardt & Madau 2012, Figure 14). By contrast, the simulation and our best fit model using $\dot{n}_{\rm ion} = \dot{N}_t$ show a decelerated change in $Q(z)$ as $Q \rightarrow 1$. This is clearly due to the fact that the ratio of ionizations to emitted photons decreases as $Q \rightarrow 1$, as illustrated in Figure 22. The consequence of this flattening in the $Q(z)$ curve is a delay in redshift of overlap of $\Delta z = 0.6$–0.8, relative to the predictions of Equations (35) and (31), respectively, using the photon injection rate as the source term.

We have seen above that the ionization rate density is the appropriate quantity to use to source the dQ/dt equation, independent of δ_b corrections. Because the ionization rate density is not directly observable, but since $\dot{n}_{\rm ion}$ can be derived from observables, we introduce a correction factor to convert from one to the other. Defining

$$\gamma \equiv \frac{\langle n_{\rm H\,I}\Gamma^{ph}_{\rm H\,I}\rangle}{\dot{n}_{\rm ion}} = \frac{\dot{N}_t}{\dot{n}_{\rm ion}}, \tag{36}$$

where the angle brackets denote an average over the singly thresholded volume (IGM), then we can recast Equation (35) into a form useful for observers:

$$\frac{dQ}{dt} = \frac{\gamma\dot{n}_{\rm ion}}{\delta_b\bar{n}_{\rm H}} - \frac{Q}{\bar{t}_{\rm rec}}, \tag{37}$$

where γ and δ_b are functions of Q. In Figure 29, we plot data values for $\gamma(Q)$ taken from our simulation, as well as a simple power-law fit. The fit is not meant to be definitive, but merely illustrative. More simulations need to be performed under various circumstances, and better fits made, to see whether our $\gamma(Q)$ is approximately universal, or merely anecdotal.

7. DISCUSSION

7.1. Significance of our Main Results

We have carried out a fully coupled radiation hydrodynamic cosmological simulation of hydrogen reionization by stellar sources using an efficient FLD radiation transport solver coupled to the *Enzo* code (Paper I). This method has the virtue of a high degree of scalability with respect to the number of sources, which allows us to simulate reionization in large cosmological volumes including hydrodynamic and radiative feedback effects self-consistently. In this paper, we have presented the first results from a simulation in a cosmological volume of modest size—20 Mpc comoving—to investigate the detailed radiative transfer, nonequilibrium photoionization, photoheating and recombination processes that operate during reionization and dictate its progress. In a future paper, we apply our method to larger volumes to examine the large-scale structure of reionization, evolution of the bubble size distribution, etc.

The simulation presented here is carried out on a uniform mesh of 800^3 cells and with an equivalent number of dark matter particles. As such, the mass resolution is sufficiently high to evolve a dark matter halo population that is complete down to ($M_{\rm halo} \approx 10^8\,M_\odot$), which cools via H and He atomic lines. However, a spatial resolution of 25 kpc comoving poorly resolves internal processes within early galaxies, but does an excellent job of resolving the Jeans length in the photoionized IGM (Bryan et al. 1999). Our simulation is most appropriately thought of as a high-redshift IGM simulation which evolves an inhomogeneous ionizing radiation field sourced by star-forming early galaxies. Star formation is modeled using a modified version of the Cen & Ostriker (1992) recipe that can be tuned to reproduce the observed SFRD (Smith et al. 2011). We have tuned our simulation to roughly match the observed SFRD (Bouwens et al. 2011a; Robertson et al. 2013) for $z \geqslant 7$, but, due to the small box size, it somewhat underpredicts the SFRD for $z < 7$. Our simulation also matches the observed $z = 6$ galaxy luminosity function well, which gives us some confidence that our ionizing source population is representative of the real universe. However, a substantial fraction of our ionizing flux comes from sources that are too faint to be observed; we defer a discussion of this topic to Paper III in this series (G. C. So et al., in preparation).

Our goal was not to predict the precise redshift of ionization completion, as this would depend on details such as the escape fraction of ionizing radiation from galaxies and their stellar populations that we do not model directly. Rather, our goal was to examine the mechanics of reionization in its early, intermediate, and late phases within a model which is calibrated to the observed source population. Nonetheless, we present a model in which reionization completes at $z \approx 6$, consistent with observations.

At early and intermediate times we find that reionization proceeds "inside-out," confirming the results of many previous investigations (Gnedin 2000a; Razoumov et al. 2002; Sokasian et al. 2003; Furlanetto et al. 2004; Iliev et al. 2006; Trac & Cen 2007; Trac et al. 2008). However, at late times isolated islands of neutral gas are ionized from the outside-in as they have no internal sources of ionization. Even this characterization is somewhat oversimplified when degree of ionization is considered, as we discussed in Section 3.2. It accurately depicts how reionization proceeds for a low degree of ionization (>0). However, for high degrees of ionization, "inside-out-middle" is

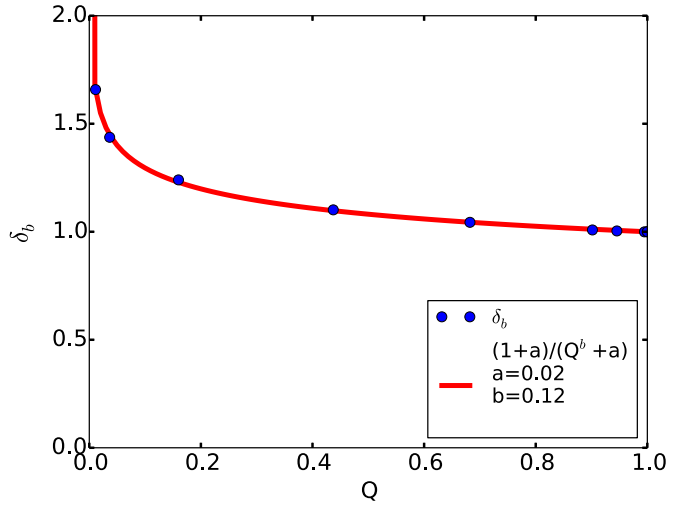

Figure 26. Mean baryon overdensity of ionized gas as a function of the ionized volume-filling fraction Q. The blue points are measured in the simulation by averaging over the doubly thresholded cells obeying $\Delta_b < 100$ and $x_e > 0.1$. The red curve is a fit to the data.

(A color version of this figure is available in the online journal.)

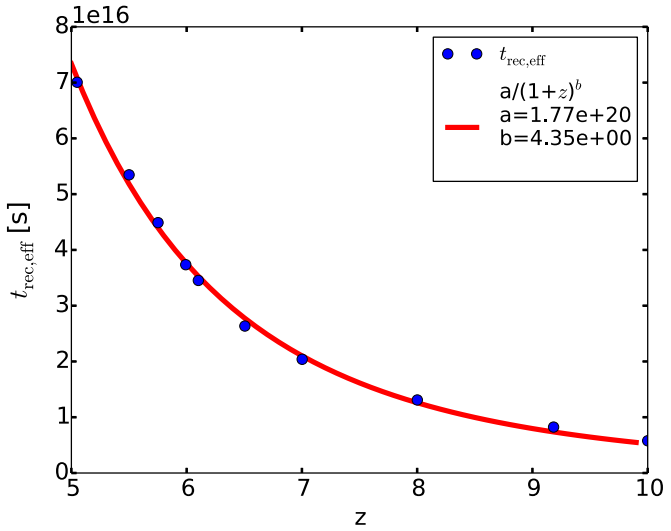

Figure 27. Analytic fit to $t_{\rm rec,eff}$ (red line), evaluated using simulation data (blue points) via Equation (34).

(A color version of this figure is available in the online journal.)

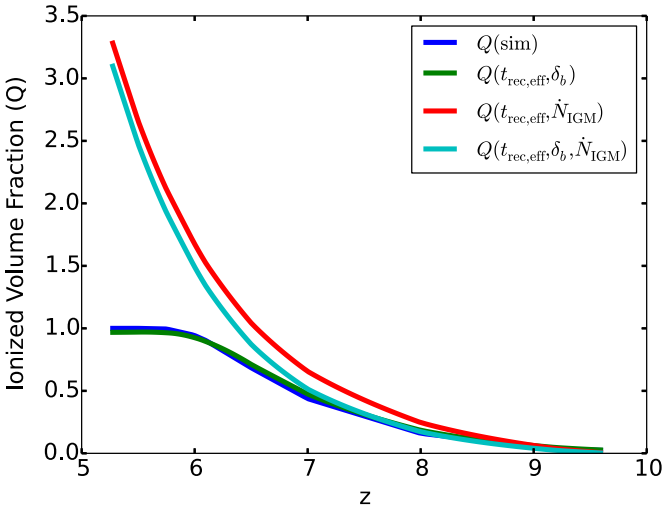

Figure 28. Dependence of analytic models on the choice for $\dot{n}_{\rm ion}$. The red and teal curves assume $\dot{n}_{\rm ion} = \dot{N}_{\rm IGM}$; i.e., the photon injection rate into the IGM. The green curve assumes $\dot{n}_{\rm ion} = \dot{N}_t$; i.e., the measured photoionization rate in the IGM. The blue curve is Q(sim)–the measured ionized volume-filling fraction in the simulation. The green and teal curves take into account the overdensity effect of inside-out reionization (Equation (37)), while the red curve assumes $\delta_b = 1$. All models assume $\bar{t}_{\rm rec} = t_{\rm rec,eff}$ as measured in the simulation (Figure 27).

(A color version of this figure is available in the online journal.)

more appropriate, as filaments lag behind low and high density regions, as discussed by Finlator et al. (2009).

Our most interesting findings concerns the widely used analytic model of reionization introduced by Madau et al. (1999). Both the instantaneous (Equation (1)) and time-dependent (Equation (31)) versions of this model underpredict the time (overpredict the redshift) when reionization completes, when applied to our simulation. There are two reasons for this which are related to the detailed mechanics of reionization at early and late times, respectively. At early times, I fronts are propagating in regions of higher density than the cosmic mean since the first sources are highly biased. Higher densities translate into slower bubble expansion rates, retarding $Q_{\rm H\,II}(z)$ relative to a solution which assumes the cosmic mean density (Figure 25). At late times, which we loosely define as $Q_{\rm H\,II} > 0.5$, conversion of ionizing photons into new ionized hydrogen atoms becomes inefficient. This can be seen by forming this ratio directly from the simulation data (Figure 22), or by defining a global H I ionization parameter (Equation (29) and Figure 20). The consequence of this dropping ionization efficiency, which is as low as 0.05 at overlap in our simulation, is to further retard $Q_{\rm H\,II}(z)$ relative to a solution which assumes an ionization efficiency of unity (Figure 28).

We have introduced a modified version of Madau et al. (1999)'s time-dependent analytic reionization model in Equation (37). Modifications that correct for the above-mentioned effects apply to the source term only, not to the recombination term. These corrections are therefore totally independent of issues like clumping factors and the temperature of the IGM, which enter into the characteristic recombination time of the IGM. The modifications are introduced as correction factors to the mean density of baryons in the vicinity of ionizing sources at early times (δ_b), and the conversion efficiency of ionizing photons emitted to H I photoionization rate at late times (γ). Fits of these two correction factors versus $Q_{\rm H\,II}$ are presented in Figures 26 and 29 for consumption by other researchers. At this point, we do not know how general these results are. However, we have indications based on another simulation we have analyzed with a softer source SED that the functional forms are representative of this class of reionization model.

The significance of these results to high-redshift galaxy observers is the following. Setting $Q_{\rm H\,II} = 1$ and $\delta_b = 1$ in Equation (37), we derive

$$\dot{n}_{\rm ion} = \frac{1}{\gamma}\frac{\bar{n}_H}{\bar{t}_{\rm rec}}. \quad (38)$$

This differs from the usual expression used to assess whether a given ionizing photon injection rate can maintain an ionized IGM by the factor $1/\gamma$, which is a factor of $\sim$20 at overlap in our simulation. If this result is correct, then it means that the required UV luminosity density to maintain an ionized IGM has been underestimated by a factor of approximately 20. However, a more precise statement would be that the UV luminosity density required to maintain the IGM in a highly ionized state;

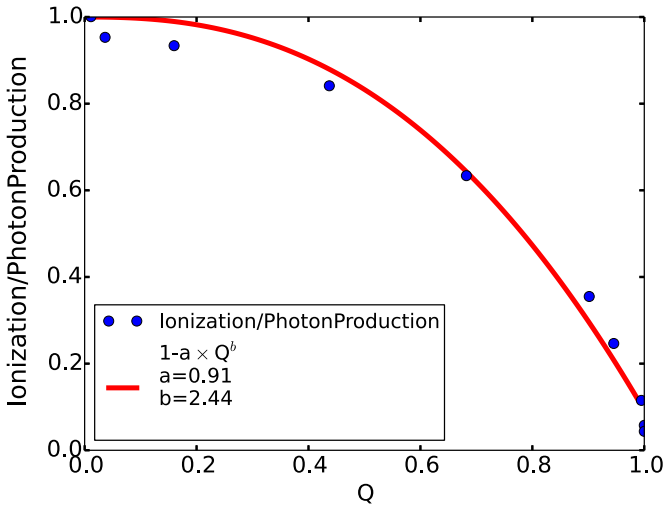

Figure 29. Ratio of the volume-averaged H I photoionization rate to photon injection rate in the IGM as a function of Q. Data points are measured from the simulation; the line is a simple power-law fit.

(A color version of this figure is available in the online journal.)

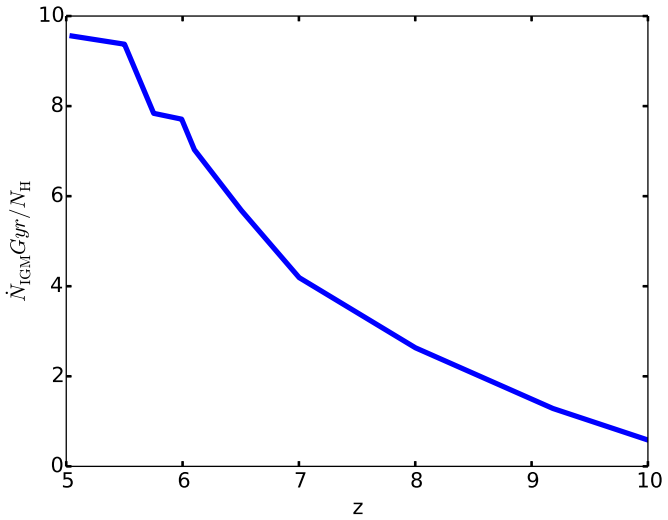

Figure 30. Instantaneous number of ionizing photons escaping into the IGM ($\dot{N}_{\rm IGM}$) per hydrogen atom per gigayear as measured in our simulation. This quantity has been estimated from observations by Becker & Bolton (2013), and found to be in the range of 2–14, with median value of 5 at $z = 4.75$. Our result is at the high end of this range but within error bars (but see discussion in the text).

(A color version of this figure is available in the online journal.)

$f_n = 10^{-5}$ is 20 times higher than what has been previously estimated. Lower levels of UV luminosity density than that specified in Equation (38) could still maintain the IGM in an ionized state, but one with a higher neutral fraction.

As we showed in Figure 24, the effective recombination time at and after overlap in our model is comparable to the Hubble time, whether we use the Madau formula to evaluate it for reasonable values for the clumping factor, or we evaluate it directly from our simulation data. This fact casts in doubt the entire instantaneous photon counting argument, which is the basis of Equation (1), and the equation becomes less useful for the purposes to which it has been applied (e.g., Robertson et al. 2013). It means that the ionization state of the IGM has a memory on the timescale of $\bar{t}_{\rm rec}$, which is always a significant fraction of $t_{\rm Hubble}$ before overlap, and of the order of the Hubble time after overlap. We therefore recommend observers use the time-dependent version Equation (37) in future assessments of high-redshift galaxy populations and their role in reionization.

7.2. Is Reionization Photon Starved?

Bolton & Haehnelt (2007) introduced the concept of photon-starved reionization. They used observations of the Lyα opacity of the IGM and the ionizing emissivity at $z \geqslant 5$ to estimate the photo-ionization rate in the post-reionization IGM. They inferred that the ionizing emissivity is roughly constant over the redshift range 2–6 and corresponds to 1.5–3 photons emitted per hydrogen atom over a period of the age of the universe at $z = 6$. Becker & Bolton (2013) have revisited this topic and using new measurements of the intensity of the UVB and the global ionizing emissivity have revised this number upward by roughly a factor of two. At $z = 4.75$, they estimate the number of ionizing photons per hydrogen atom per gigayear is in the range of 2–14, with a median value of 5. In Figure 30, we plot this quantity as measured in our simulation. Our result is at the high end of this range but within error bars. This agreement is perhaps fortuitous, since our simulation does not include an explicit escape factor. As discussed below, our limited resolution prevents an accurate calculation of the absorption of ionizing photons by the ISM of the galaxies themselves. However, we do calculate a mean absorption due to circumgalactic gas resolved on our mesh, and express this as $f_{\rm esc}({\rm CGM}) \approx 0.7$ (Section 5).

Current estimates for the total ionizing escape fraction of high-redshift galaxies are very uncertain, but it likely far less than this number by a factor of 5–10 (see the discussion in Wise et al. (2014)). Incorporating this correction would reduce our estimate proportionately. However, our SFRD underestimates the observed value by 2.5 times at $z = 5$ due to finite box size effects. Correcting for both effects would drop our estimate of the number of ionizing photons per hydrogen atom per Gyr at $z = 5$ by a factor of 2–4, closer to the median value of Becker & Bolton (2013).

7.3. Limitations of the Simulation

We conclude this section with a brief discussion of the known limitations of our simulation and a comparison of our results with others in the published literature. First, we discuss the limitations. The principal limitation is the use of a uniform grid, which prevents us from resolving processes occurring inside galaxy halos. The main defect this introduces is an inability to calculate the ionizing escape fraction directly, as is done in some high-resolution simulations; e.g., Wise & Cen (2009), Fernandez & Shull (2011). In our simulation, we calibrate our star formation recipe to match the observed SFRD, and then use that that to calculate UV feedback cell-by-cell via Equation (15). We use a value for $\epsilon_{\rm UV}$ taken from Ricotti et al. (2002) for an unattenuated low metallicity stellar population. We underestimate the amount of internal attenuation of ionizing flux due to our limited resolution within halos, and we do not incorporate an explicit escape fraction parameter in Equation (15). Effectively, we assume $f_{\rm esc}({\rm ISM}) = 1$. Using a lower value for $f_{\rm esc}$ would result in a lower overlap redshift (Petkova & Springel 2011). Clearly, it would be desirable to vary this parameter in future studies.

Our use of a uniform grid also prevents us from resolving Lyman limit systems (LLS), which are an important source of Lyman continuum opacity post-overlap. As discussed in McQuinn et al. (2011), the evolution of the UVB intensity post-overlap depends sensitively on the presence of such systems. LLS are absent in our simulation, and therefore the post-overlap

evolution is not trustworthy. Before overlap, the presence of LLS may influence the duration of reionization epoch through their contribution to the clumping factor of the IGM (McQuinn et al. 2011). We are investigating this through a series of higher-resolution simulations that will be reported on in a future work.

A second limitation of our simulation is that we have presented only one realization in a relatively small box. Previous studies have shown that H II bubbles reach a characteristic size of ~10 Mpc comoving in the late stages of reionization (Furlanetto et al. 2004; Zahn et al. 2007; Shin et al. 2008). At 20 Mpc on a side, our box is scarcely larger than this. Therefore, one can ask how robust our results are to box size. We have addressed this by carrying out a simulation of identical physics, spatial, and mass resolution in a volume 64 times as large as the one described in this paper. The simulation is carried out in a box 80 Mpc on a side on a uniform mesh of 3200^3 cells, and with an equivalent number of dark matter particles. Results of this simulation will be presented in a forthcoming paper (G. C. So et al., in preparation). For the present, we merely state that the $Q_{\rm H\,II}(z)$ curve for the 800^3 simulation falls within the $\pm 1\sigma$ band for the larger simulation, where this band is obtained by subdividing the large simulation into 64 cubes of size 20 Mpc on a side, and calculating the mean and standard deviation. While the larger box begins to ionize at a slightly earlier redshift, due to the presence of higher sigma peaks forming galaxies, both simulations complete reionization at the same redshift, $z_{\rm reion} = 5.8$. The $Q_{\rm H\,II}(z)$ curve for the 800^3 simulation is near the lower edge of the band, which means that at intermediate redshifts ($7 \leqslant z \leqslant 8$), where the difference is largest, the small box simulation underestimates the fraction of the volume that is ionized by about 20%, with differences smoothly decreasing to lower and higher redshift.

A third limitation is that our SFRD systematically deviates from observations below $z \sim 7$, flattening and then decreasing slightly, rather than continuing to rise (Figure 3). The large box simulation does not show this effect, but rather tracks the observed SFRD over the entire range of redshifts. The difference in the mean SFRD between the large and small box simulations increases smoothly from 0.1 dex at $z = 9$ to 0.3 dex at $z = 6$. The higher levels of star formation in the large box simulation accounts for the higher ionized volume fraction at intermediate redshifts. Nonetheless, the two simulations complete reionization at virtually the same redshift, which is a curious result which we address in a subsequent paper.

Another limitation of our method is the use of FLD to transport radiation. It is well known that FLD does not cast shadows behind opaque blobs. This could potentially overestimate how rapidly the IGM ionizes, and hence overestimate $z_{\rm reion}$. Of particular importance to the results presented in this paper is the treatment of neutral gas in regions of moderate overdensities $10 \leqslant \delta_b \leqslant 100$. To investigate the importance of shadowing in large-scale reionization simulations, in the Appendix we present a detailed comparison of FLD and ray tracing results on a fully coupled cosmological reionization test problem of our own design. We see some minor differences in the ionized volume and mass fractions and phase diagrams at an early stage of reionization for gas of moderate overdensities which could indicate excess amounts of ionization by FLD compared to ray tracing. However, we see these differences diminish as reionization progresses. We do not claim that our result is converged, as this is beyond the limits of what is currently possible to simulate by our method and others. However, the good agreement between FLD and ray tracing at late times in our test problem demonstrates that the results are reliable to the extent of the mass and spatial resolution employed. Exploring the fate of denser gas embedded in ionized regions will require simulations of higher resolution to what we have presented, and are planned as follow-ons to the present work.

7.4. Comparison with Other Self-Consistent Simulations

Finally, we compare our results to the results of several recent fully coupled simulations of reionization including hydrodynamics, star formation, and radiative transfer. Petkova & Springel (2011) simulated a (10 Mpc h^{-1})^3 volume with the `Gadget-2` code coupled to a variable tensor Eddington factor moment method for the ionizing radiation field sourced by star forming galaxies. They carried out a suite of simulations with 2×128^3 gas and dark matter particles, varying the ionizing escape fraction and the mean energy per photon from hot, young stars. They also performed one simulation at 2×256^3 resolution to check for convergence. Our simulation has 80/10 times superior mass resolution as their $128^3/256^3$ simulations. Because `Gadget` is a Lagrangian code, our Eulerian simulation has 8/16 times lower resolution in the highest density regions, but 4.46/2.23 times higher resolution at mean density, and even higher resolution compared to the `Gadget` simulations in low density voids. Our method also has a more accurate adaptive subcycling timestepping scheme for the coupled radiation-ionization-energy equations, obviating the need to model nonequilibrium effects by means of a gas heating parameter ϵ.

Morphologically, our results are qualitatively similar, as are the neutral hydrogen fraction versus overdensity phase diagrams. As might be expected from the two methods, the phase diagrams show some differences at the highest and lowest overdensities, which is likely a resolution effect. The SFRD in the Petkova & Springel (2011) simulation is about an order of magnitude higher than observed, making a direct comparison on $Q_{\rm H\,II}(z)$ somewhat problematic. However, since they vary the ionizing escape fraction, we can roughly compare their $f_{\rm esc} = 0.1$ case with our results. Their model completes reionization at $z \approx 5$ compared to our own which completes at $z \approx 5.8$. They plot the quantity $\log[1 - Q_{\rm H\,II}(z)]$, which makes the end of reionization look abrupt. We plot $Q_{\rm H\,II}(z)$, which makes the end of reionization look slow. When we plot $\log[1 - Q_{\rm H\,II}(z)]$ using our data, it looks very similar to their curves, and shows a rapid plunge in the average neutral fraction at late times. Petkova & Springel (2011) do not compare with the predictions of the Madau et al. (1999) model, nor do they investigate the evolution of clumping factors, recombination times, or the number of photons per H atom to achieve overlap as we do. We do not investigate the properties of the $z = 3$ IGM via Lyα forest statistics, as they do. Therefore, further comparisons are not possible at this time.

Finlator et al. (2012) examined some of the same issues we have, and hence a comparison with their results is informative. They carried out a suite of `Gadget-2` simulations in small volumes (3, 6) Mpc h^{-1} coupled to a variable tensor Eddington factor moment method. Unlike Petkova & Springel (2011), the radiation transport is solved on a uniform Cartesian grid, rather than evaluated using the smoothed particle hydrodynamics formalism. The results presented in Finlator et al. (2012) use 2×256^3 dark matter and gas particles, which, given their small volumes, yields a similar mass resolution to our simulation,

superior spatial resolution in high density regions, and slightly coarser spatial resolution at mean density and below. However, their radiation transport is done on coarse 16^3 mesh, which in their fiducial run is 536 comoving kpc ≈20 times as coarse as ours. Their simulation thus coarse-grains the radiation field relative to the density field, which necessitates the introduction of a sub (radiation) grid model for unresolved self-shielded gas (i.e., Lyman limit systems). The effect of their subgrid model is to remove some gas in the overdensity regime $1 \leqslant \Delta_b \leqslant 50$ in the calculation of the H II clumping factor, thereby lowering it. Since our radiation field is evolved on the same grid as the density field, we have not included an explicit subgrid model for unresolved self-shielded gas. Lyman limit systems, with neutral column densities of $\sim 10^{17}$ cm^{-2}, have a characteristic size of 10 physical kpc (Schaye 2001; McQuinn et al. 2011). At $z = 6$ this is 70 comoving kpc, which is resolved by three grid cells in our simulation. While this is lower than one would ideally like (5–10 cells), we believe we can make an apples-to-apples comparison between our resolution-matched simulation results and Finlator et al.'s results.

Our results are in broad agreement with those of Finlator et al. (2012), with some minor quantitative differences. We both find that the unthresholded baryon clumping factor C_b significantly overestimates the clumping in ionized gas at redshifts approaching overlap, and therefore that it should not be used to estimate the mean recombination rate in the IGM. We confirm their findings that properly accounting for the ionization state and temperature of gas of moderate overdensities lowers the clumping factor to less than ≈6 (in our case less than 5; see Figure 17). Finlator et al. quote a value for $C_{\rm H\,II}$ of 4.9 at $z = 6$ taking self-shielding into account, which is in good agreement with our value of $C_{\rm ttH\,II} \approx 4.8$. However, they favor a lower value for C of 2.7–3.3, taking temperature corrections into account. This can be compared with our value for $C_{\rm RR} \approx 2.3$, which includes temperature corrections but also excludes gas with $\Delta_b < 1$. Including this low-density gas, as Finlator et al. do, would raise this value somewhat since a larger range of densities enter into the average. We conclude therefore that clumping factors derived from our simulation are in good agreement with those reported by Finlator et al. (2012).

We find that approximately two photons per hydrogen atom ($\gamma/H \approx 2$) are required to reionize gas satisfying $\Delta_b < 100$–our proxy for the fluctuating IGM. Finlator et al. (2012) quote a model-dependent value for γ/H which depends on the redshift at which the IGM becomes photoheated and thereby Jeans smoothed (their Figure 7). For $z = 6$, $\gamma/H \approx 5$, significantly higher than our number evaluated directly from the simulation. However, for $z = 8$, when our box is already significantly ionized, $\gamma/H \approx 3$. Because there are many model-dependent assumptions that go into the Finlator et al. estimate, we consider this reasonably good agreement. However, we point out that our estimate is the first to be derived from a self-consistent simulation of reionization with no subgrid models aside from the star formation/radiative feedback recipe.

Finally, Finlator et al. (2012) compare $Q_{\rm H\,I}(z) = 1 - Q_{\rm H\,II}(z)$ for their fiducial model with the time-dependent model of Madau et al. (1999). They point out the sensitivity of the redshift of overlap on the choice of clumping factor, which enters into the recombination time, and showed that $C_{\rm H\,II}$ provides better agreement with theory at early times than C_b, consistent with our findings. Since small discrepancies in $Q_{\rm H\,II}(z)$ at early times are masked by plotting $Q_{\rm H\,I}(z)$, Finlator et al. did not discover the need for our overdensity correction δ_b. Similar to us, they found that even with the best clumping factor estimate the analytic model predicts that reionization completes earlier than the simulation by $\Delta z \approx 1$. They ascribe this delay to finite speed-of-light effects (which can only account for $\Delta z = 0.1$), while we ascribe it to nonequilibrium ionization effects. Finlator et al. (2012) did not propose modifications to the Madau et al. (1999) model to improve agreement with simulation, as we do in Equation (37).

8. SUMMARY AND CONCLUSIONS

We now summarize our main results.

1. We use a fully self-consistent simulation including self-gravity, dark matter dynamics, cosmological hydrodynamics, chemical ionization, and FLD radiation transport, to look at the epoch of hydrogen reionization in detail. By tuning our star formation recipe to approximately match the observed high-redshift star formation rate density and galaxy luminosity function, we have created a fully coupled radiation hydrodynamical realization of hydrogen reionization which begins to ionize at $z \approx 10$ and completes at $z \approx 5.8$ without further tuning. While our goal is not the detailed prediction of the redshift of ionization completion, the simulation is a realistic enough to analyze in detail the role of recombinations in the clumpy IGM on the progress of reionization.
2. We find that roughly two ionizing photons per H atom are required to convert the neutral IGM to a highly ionized state.
3. Reionization proceeds initially "inside-out," meaning that regions of higher mean density ionize first, consistent with previous studies. However the late stages of reionization are better characterized as "outside-in" as isolated neutral islands are swept over by externally driven I fronts. Intermediate stages of reionization exhibit both characteristics as I fronts propagate from dense regions to voids to filaments of moderate overdensity. In general, the appropriateness of a given descriptor depends on the level of ionization of the gas, and the reionization process is rather more complicated that these simple descriptions imply.
4. The evolution of the ionized volume fraction with time $Q_{\rm H\,II}(z)$ depends on the level of ionization chosen to define a parcel of gas as ionized. The curves for ionization fractions $f_i = 0.1$ and $f_i = 0.999$ are very similar, but the curve for $f_i = 0.99999$ is significantly lower at a given redshift, amounting to a delay of $\Delta z \approx 1$ relative to the other curves for $Q_{\rm H\,II} \ll 1$, smoothly decreasing to 0 as the redshift of overlap is approached.
5. Before overlap, 30%–40% of the total recombinations occur outside halos in our simulation, where this refers to gas with $\Delta_b < 100$. After overlap, this fraction decreases to 20% and continues to decrease to lower redshifts.
6. Before and after overlap, 3%–4% of the total recombinations occur in voids (defined as $\Delta_b < 1$.) While this is a small fraction of all recombinations, it is about 10% of recombinations before overlap, increasing to about 20% by $z = 5$. The contribution of voids to the ionization balance of the IGM is therefore not negligible.
7. The formula for the ionizing photon production rate needed to maintain the IGM in an ionized state derived by Madau et al. (1999; Equation (1)) should not be used to predict the epoch of reionization completion because it ignores history-dependent terms in the global ionization balance

that are not ignorable. While not originally intended for this purpose, it is being used by observers to assess whether increasingly higher redshift populations of star-forming galaxies can account for the ionized state of the IGM. A direct application of the formula to our simulation predicts an overlap redshift of $z = 7.4$ compared to the actual value of $z = 5.8$.

8. Estimating the recombination rate density in the IGM before overlap through the use of clumping factors based on density alone is unreliable because it ignores large variations in local ionization state and temperature which increase the effective recombination time compared to density-based estimates. For a currently popular value of the clumping factor $C = 3$ (Shull et al. 2012), the formula for $\bar{t}_{\rm rec}$ from Madau et al. (1999; Equation (21)) underestimates by two times at all redshifts the effective recombination time measured directly from the simulation. If we adjust C downward so that Equation (21) matches $t_{\rm rec,eff}$ from the simulation, then it is too low by 60% at $z = 6$ due to the aforementioned effects.
9. The assumption that $\bar{t}_{\rm rec}/t \ll 1$ which Madau et al. (1999) assumed to derive Equation (1) is never valid over the range of reionization redshifts explored by our simulation (Figure 24). Depending on how $\bar{t}_{\rm rec}$ is evaluated, $\bar{t}_{\rm rec}/t$ increases from 0.3–0.4 at $z = 9.7$ to $\geqslant 1$ at overlap. Nonetheless, Equation (1) remains true on a timescale $\bar{t}_{\rm rec}$ after overlap. This means that observers should exercise caution using an instantaneous ionizing photon production rate in Equation (1) to determine whether the observed source population is capable of maintaining the IGM in an ionized state.
10. Retaining time-dependent effects is important for the creation of analytic models of global reionization. The analytic model for the evolution of $Q_{\rm H\,II}$ introduced by Madau et al. (1999; Equation (31)) retains important time-dependent effects, and predicts well the shape of our simulated curve, but overpredicts $Q_{\rm H\,II}$ at all redshifts because it does not take into account that reionization begins in overdense regions consistent with the inside-out paradigm. It also assumes every emitted ionizing photon results in a prompt photoionization, which is not true in our simulation at late times $Q_{\rm H\,II} > 0.5$. The Madau model, which ignores these effects, predicts a universe which reionizes too soon by $\Delta z \approx 1$. When we introduce correction factors for these effects into Equation (37) the simulation and model curves agree to approximately 1% accuracy. We recommend researchers use Equation (37) for future analytic studies of reionization.
11. Finally, we present in Figures 26, 27, and 29 fitting functions for the overdensity correction $\delta_b(Q)$, the effective recombination time derived from our simulation, and the ionization efficiency parameter $\gamma(Q)$ which may be useful for other researchers in the field.

This research was partially supported by National Science Foundation grants AST-0808184 and AST-1109243 and Department of Energy INCITE awards AST025 and AST033 to M.L.N. and D.R.R. J.H.W. acknowledges support from NSF grants AST-1211626 and AST-1333360. Simulations were performed on the *Kraken* supercomputer operated for the Extreme Science and Engineering Discovery Environment (XSEDE) by the National Institute for Computational Science (NICS), ORNL with support from XRAC allocation MCA-TG98N020 to M.L.N. M.L.N., D.R.R., and G.S. especially acknowledge the tireless devotion to this project by our co-author Robert Harkness, who passed away shortly before this manuscript was completed.

APPENDIX

COMPARING FLD AND RAY TRACING

In this Appendix, we compare the results of our *Enzo+FLD* method on a cosmological reionization test problem to those obtained using *Enzo+Moray* (Wise & Abel 2011), which implements adaptive ray tracing for the transport of ionizing radiation. We examine the evolution of the ionized mass and volume as well as 2D histograms of H I and gas temperature versus baryon overdensity using both methods to ascertain whether FLD's well-known inability to cast shadows has an influence on the progress of reionization.

The test problem is a scaled down version of the simulation described in Section 2.1, which is identical to it in all respects except that the simulated volume is a cube 6.4 comoving Mpc on a side, computed on a grid of 256^3 cells and an equivalent number of dark matter particles. The test problem thus has the same mass and spatial resolution as the 20 comoving Mpc, 800^3 simulation presented in the main body of the paper. Initial conditions were generated in the same way as described in Section 2.1 and used to initialize both *Enzo+FLD* and *Enzo+Moray* simulations. Star formation and feedback is done using the same method for both simulations as described in Section 2.4; indeed, the same subroutine is called by both simulations. For the purposes of this test problem, we assume a monochromatic radiation field with photon energy $h\nu = 21$ eV.

The FLD simulation was evolved to a stopping redshift of $z = 5$; it consumed 4.8 wall-hours on 256 cores of the *Stampede* HPC cluster at the Texas Advanced Computing Center. The ray tracing simulation was run to a stopping redshift of $z \approx 7.5$—before complete reionization—after it had consumed nearly 200 wall-hours on 128 core AMD cluster at Georgia Tech (Figure 31(a)). The FLD simulation is thus more than 15 times faster than the *Moray* simulation on this problem due to the large number of ionization sources and load imbalance issues on a unigrid calculation, even after differences in processor speed are taken into account. This makes FLD an attractive alternative to ray tracing for large scale reionization simulations.

In Figure 31(b), we plot the evolution of the stellar mass, showing that the differences between the two numerical radiative transfer approaches do not significantly affect the star formation history in the simulation. The stellar masses agree to within 10% at $z \approx 7.5$ when the *Moray* calculation is terminated.

In Figure 32(a), we show the evolution of the volume and mass fractions of H I that is more than 10% ionized, in the cosmological reionization test problem for the two simulation methods. The *Moray* calculation is terminated when the volume is ~80% ionized because the computation becomes very costly in cpu-time as the volume becomes transparent and covered with rays. Generally, there is good agreement between the two simulations, with the FLD solution ionizing slightly faster than the ray tracing solution. The volume-weighted and mass-weighted curves from the FLD simulation track one another closely, whereas the mass-weighted curve slightly lags the volume-weighted curve in the *Moray* simulation. This could be an indication that higher density gas remains neutral somewhat longer in the *Moray* simulation compared to the

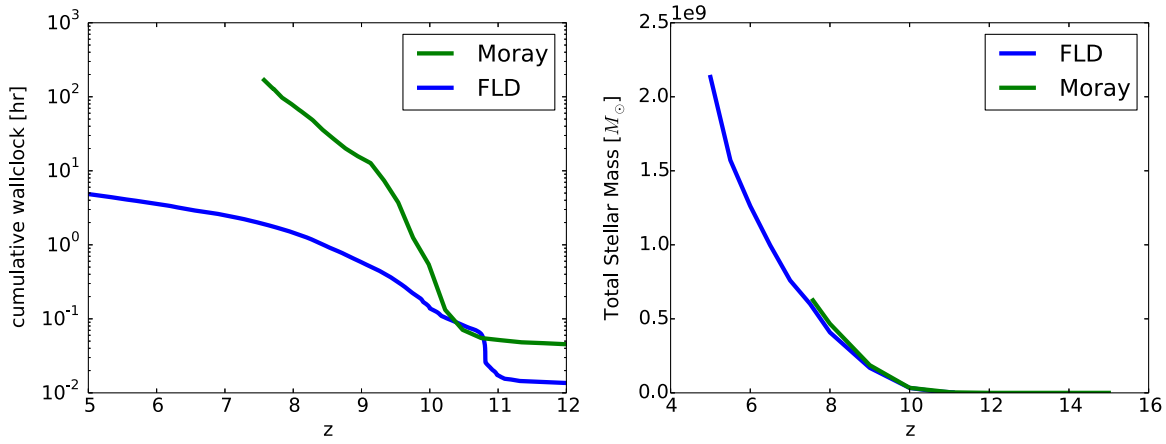

(a) (b)

Figure 31. (a) Wall time vs. redshift in cosmological reionization test problem as simulated with two different methods for the transport of ionizing radiation: flux-limited diffusion (FLD) and adaptive ray tracing (Moray), run on two different clusters with different processors (see the text). (b) Evolution of stellar mass with redshift.

(A color version of this figure is available in the online journal.)

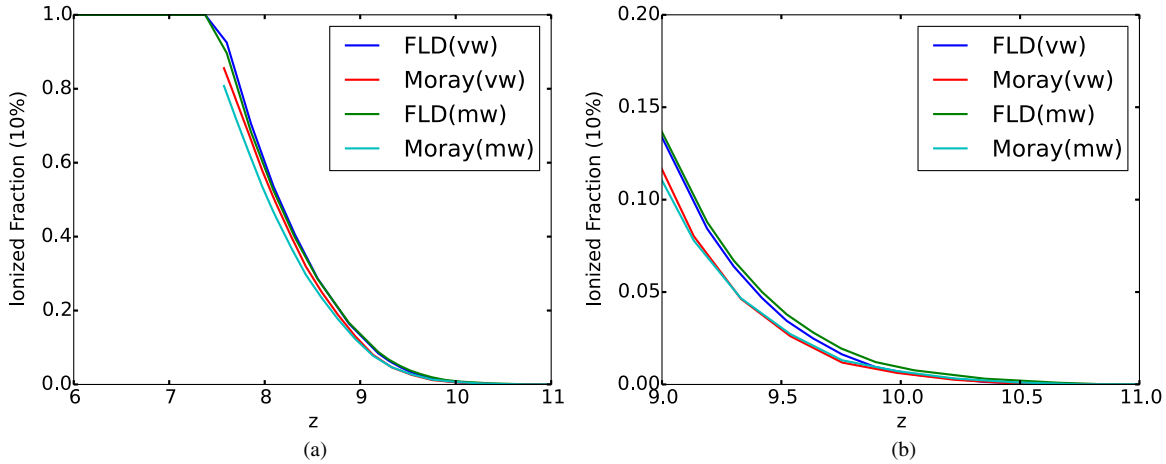

(a) (b)

Figure 32. Evolution of the ionized fraction in the cosmological reionization test problem as simulated with two different methods for the transport of ionizing radiation: flux-limited diffusion (FLD) and adaptive ray tracing (Moray). (a) Full evolution; (b) zoom-in of early stages of reionization. Volume-weighted (vw) and mass-weighted (mw) curves are plotted for gas with an ionization fraction of $\geqslant$10%.

(A color version of this figure is available in the online journal.)

FLD simulation. In Figure 32(b) we show a blowup of the early stages of reionization. We see that the FLD simulation reionizes somewhat faster than the *Moray* simulation. However, the difference in the ionized volume does not continue to grow, as we can see from Figure 32(a). A possible explanation for this behavior is that shadowing is important at early times when one luminous source dominates the reionization process. However at later times, when the ionized volume approaches unity, neutral gas embedded in ionized regions is illuminated from multiple directions, which is a circumstance FLD approximates well.

To investigate this further, we plot in Figure 33(a) 2D phase diagram of H I faction versus baryon overdensity for the two methods at three redshifts: $z = 10, 9, 8$. As redshift decreases, more of the gas becomes ionized to form a cloud of points at $f_{\rm H\,I} \sim 10^{-4}$–$10^{-3}$ and $\Delta_b = 0.1$–10. While the phase diagrams are quite similar to one another in overall appearance at each redshift, the differences are most apparent at $z = 10$, where we see the ionized cloud extending to somewhat higher overdensities in the FLD simulation as compared to the *Moray* simulation. This could be an effect of shadowing at early times. At later times these differences become less pronounced but still present.

In Figure 34, we plot temperature–overdensity phase diagrams corresponding to the panels in Figure 33. Here the agreement between the two simulations at all redshifts is very good. The locus of points at the bottom edge of the cloud of heated gas represents neutral gas at various overdensities. Interestingly, the location of the tip of this locus at high overdensities $\Delta_b \approx 100$ agrees quite well for the two simulations, indicating that gas at these densities remains neutral in both simulations. Although the location of this tip is likely the consequence of virial heating and not photoheating, the fact that both simulations have it argues against an interpretation that FLD overionizes dense gas.

Our conclusion, based on these analyses, is that despite small differences at early times, both FLD and ray tracing predict similar evolutions for the gas and that any effects due to shadowing, or the lack thereof, are of minor consequence to the progress of the global ionization state. Finally, FLD has a

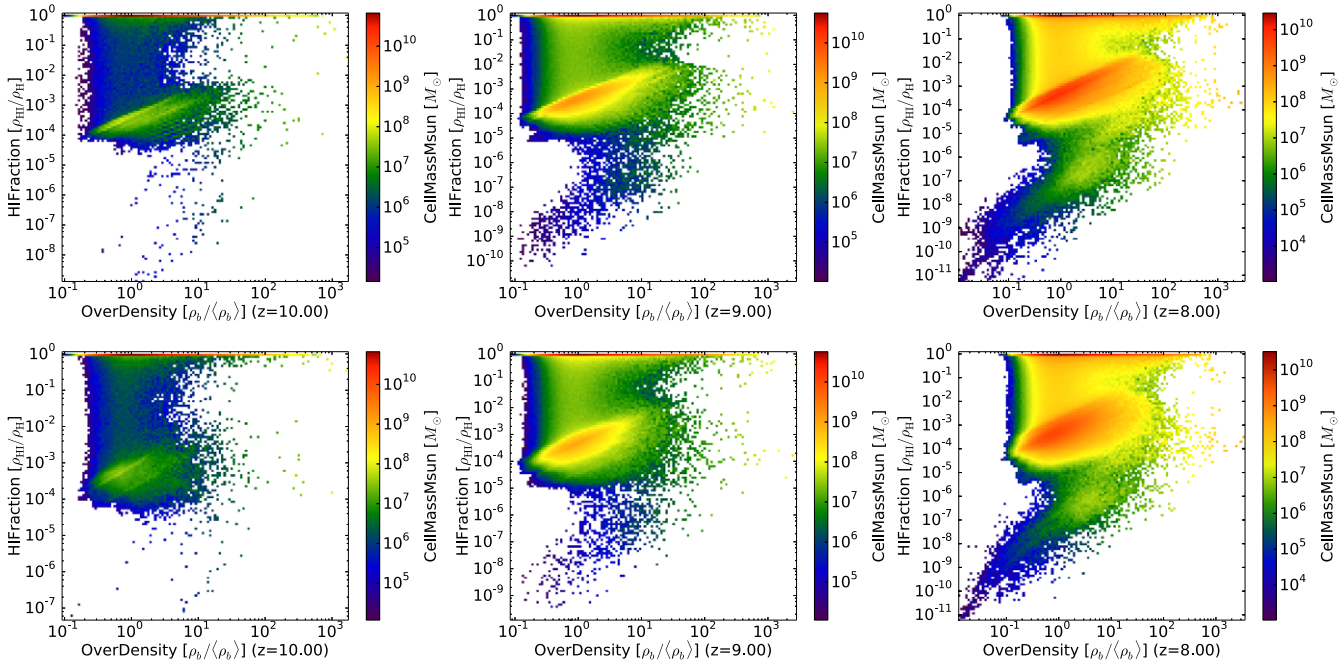

Figure 33. Phase diagram of neutral hydrogen fraction vs. baryon overdensity with decreasing redshift from left to right. Top row: FLD results; Bottom row: ray tracing results.

(A color version of this figure is available in the online journal.)

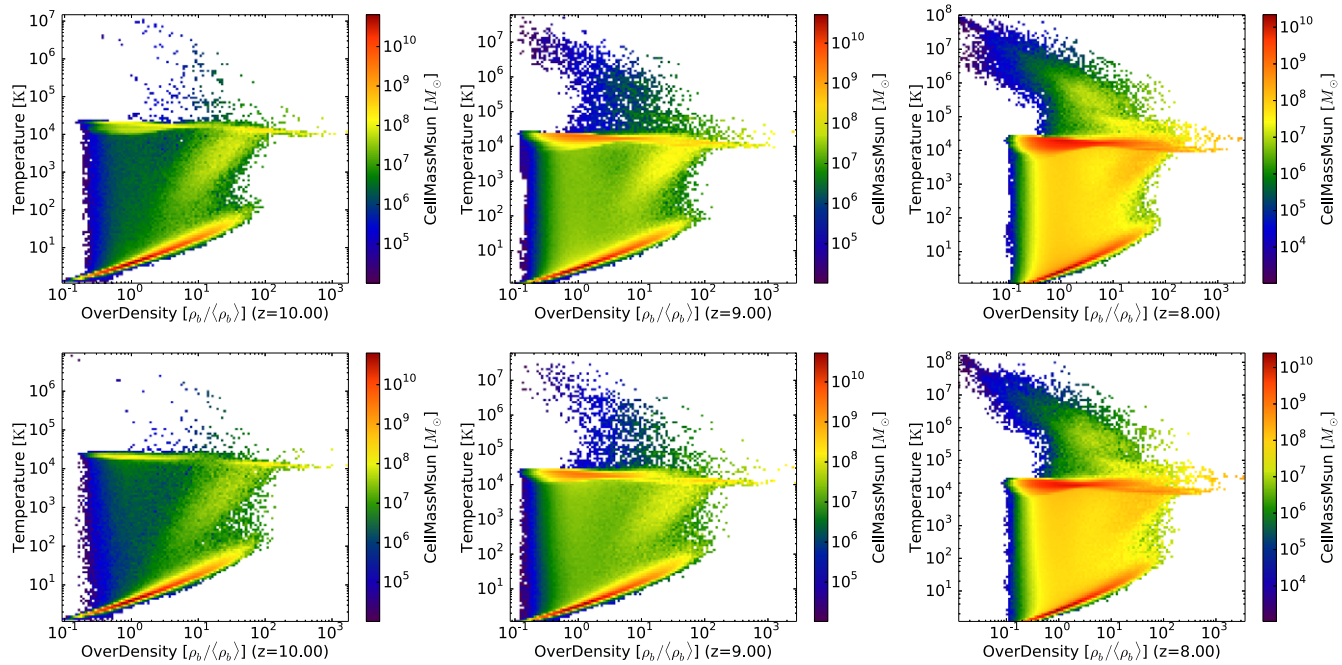

Figure 34. Phase diagram of gas temperature vs. baryon overdensity with decreasing redshift from left to right. Top row: FLD results; Bottom row: ray tracing results.

(A color version of this figure is available in the online journal.)

substantial speed advantage over *Moray*, especially at late times when a large fraction of the volume is transparent.

Note Added in Proof. As this paper went to press, the authors were contacted by P. Madau, who questioned the cause for the drop of ionization efficiency as overlap is approached, as shown in Figures 19 and 22 and discussed in Section 5. He suggested that this was due to "leakage" of photons from our relatively small box as it became transparent and suggested that a sufficiently large box would not show this effect. Since we assume periodic boundary conditions that prevent leakage, there must be another explanation. Moreover, a simulation with the same resolution and physics model but in an 80 co-moving Mpc box shows the same effect. Another possibility is that there is not sufficient absorption of Lyman continuum radiation by Lyman limit systems (LLS), which are unresolved in our simulation. We are investigating this suggestion by performing simulations of higher mass and spatial resolution. The reduced ionization efficiency as overlap is approached results in the

observed flattening the $Q(z)$ curve with respect to the Madau et al. (1999) analytic model, as shown in Figure 28 and discussed in Section 6. It is an open question whether additional opacity sources such as LLS would lead to better agreement. Until this issue is settled, our Conclusion 10 must be viewed as tentative.

REFERENCES

Abel, T., Anninos, P., Zhang, Y., & Norman, M. L. 1997, NewA, 2, 181
Abel, T., & Haehnelt, M. G. 1999, ApJL, 520, L13
Ahn, K., Iliev, I. T., Shapiro, P. R., et al. 2012, ApJL, 756, L16
Barkana, R., & Loeb, A. 2007, RPPh, 70, 627
Becker, G. D., & Bolton, J. S. 2013, MNRAS, 436, 1023
Bolton, J. S., & Haehnelt, M. G. 2007, MNRAS, 382, 325
Bouwens, R. J., Illingworth, G. D., Franx, M., & Ford, H. 2007, ApJ, 670, 928
Bouwens, R. J., Illingworth, G. D., Labbe, I., et al. 2011a, Natur, 469, 504
Bouwens, R. J., Illingworth, G. D., Oesch, P. A., et al. 2011b, ApJ, 737, 90
Bouwens, R. J., Illingworth, G. D., Oesch, P. A., et al. 2012, ApJL, 752, L5
Bryan, G. L., Machacek, M., Anninos, P., & Norman, M. L. 1999, ApJ, 517, 13
Bryan, G. L., Norman, M. L., O'Shea, B. W., et al. 2014, ApJS, 211, 19
Bryan, G. L., Norman, M. L., Stone, J. M., Cen, R., & Ostriker, J. P. 1995, CoPhC, 89, 149
Cen, R., & Ostriker, J. P. 1992, ApJL, 399, L113
Ciardi, B., Stoehr, F., & White, S. D. M. 2003, MNRAS, 343, 1101
Cowie, L. L., Barger, A. J., & Trouille, L. 2009, ApJ, 692, 1476
Eisenstein, D. J., & Hu, W. 1999, ApJ, 511, 5
Ellis, R. S., McLure, R. J., Dunlop, J. S., et al. 2013, ApJL, 763, L7
Fan, X., Carilli, C. L., & Keating, B. 2006, ARA&A, 44, 415
Fernandez, E. R., & Shull, J. M. 2011, ApJ, 731, 20
Finlator, K., Oh, S. P., Özel, F., & Davé, R. 2012, MNRAS, 427, 2464
Finlator, K., Özel, F., Davé, R., & Oppenheimer, B. D. 2009, MNRAS, 400, 1049
Furlanetto, S. R., Zaldarriaga, M., & Hernquist, L. 2004, ApJ, 613, 1
Gnedin, N. Y. 2000a, ApJ, 535, 530
Gnedin, N. Y. 2000b, ApJ, 542, 535
Gnedin, N. Y., & Ostriker, J. P. 1997, ApJ, 486, 581
Haardt, F., & Madau, P. 2012, ApJ, 746, 125
Hockney, R. W., & Eastwood, J. W. 1988, Computer Simulation Using Particles, (New York: Taylor & Francis)
Hui, L., & Gnedin, N. Y. 1997, MNRAS, 292, 27
Iliev, I. T., Mellema, G., Pen, U.-L., et al. 2006, MNRAS, 369, 1625
Jarosik, N., Bennett, C. L., Dunkley, J., et al. 2011, ApJS, 192, 14
Komatsu, E., Dunkley, J., Nolta, M. R., et al. 2009, ApJS, 180, 330
Labbé, I., González, V., Bouwens, R. J., et al. 2010, ApJL, 708, L26
Madau, P., Haardt, F., & Rees, M. J. 1999, ApJ, 514, 648
McQuinn, M., Oh, S. P., & Faucher-Giguère, C.-A. 2011, ApJ, 743, 82
Miralda-Escudé, J., Haehnelt, M., & Rees, M. J. 2000, ApJ, 530, 1
Mitra, S., Ferrara, A., & Choudhury, T. R. 2013, MNRAS, 428, L1
Morel, J. E. 2000, JQSRT, 65, 769
Norman, M. L., Reynolds, D. R., So, G. C., & Harkness, R. P. 2013, arXiv:1306.0645
Oesch, P. A., Bouwens, R. J., Illingworth, G. D., et al. 2014, ApJ, 786, 108
Osterbrock, D. E., & Ferland, G. J. 2006, Astrophysics of Gaseous Nebulae and Active Galactic Nuclei (2nd ed.; Herndon, VA: University Science Books), 38
Ouchi, M., Shimasaku, K., Furusawa, H., et al. 2010, ApJ, 723, 869
Pawlik, A. H., Schaye, J., & van Scherpenzeel, E. 2009, MNRAS, 394, 1812
Petkova, M., & Springel, V. 2009, MNRAS, 396, 1383
Petkova, M., & Springel, V. 2011, MNRAS, 412, 935
Planck Collaboration, Ade, P. A. R., Aghanim, N., et al. 2013, arXiv:1303.5076
Pritchard, J. R., & Loeb, A. 2012, RPPh, 75, 086901
Raicevic, M., & Theuns, T. 2011, MNRAS, 412, L16
Razoumov, A. O., Norman, M. L., Abel, T., & Scott, D. 2002, ApJ, 572, 695
Reynolds, D. R., Hayes, J. C., Paschos, P., & Norman, M. L. 2009, JCoPh, 228, 6833
Ricotti, M., Gnedin, N. Y., & Shull, J. M. 2002, ApJ, 575, 33
Robertson, B. E., Ellis, R. S., Dunlop, J. S., McLure, R. J., & Stark, D. P. 2010, Natur, 468, 49
Robertson, B. E., Furlanetto, S. R., Schneider, E., et al. 2013, ApJ, 768, 71
Schaye, J. 2001, ApJ, 559, 507
Schenker, M. A., Ellis, R. S., Konidaris, N. P., & Stark, D. P. 2014, arXiv:1404.4632
Schenker, M. A., Robertson, B. E., Ellis, R. S., et al. 2013, ApJ, 768, 196
Schenker, M. A., Stark, D. P., Ellis, R. S., et al. 2012, ApJ, 744, 179
Schmidt, K. B., Treu, T., Trenti, M., et al. 2014, ApJ, 786, 57
Shapiro, P. R., Giroux, M. L., & Babul, A. 1994, ApJ, 427, 25
Shapiro, P. R., Iliev, I. T., & Raga, A. C. 2004, MNRAS, 348, 753
Shin, M.-S., Trac, H., & Cen, R. 2008, ApJ, 681, 756
Shull, J. M., Harness, A., Trenti, M., & Smith, B. D. 2012, ApJ, 747, 100
Skory, S., Turk, M. J., Norman, M. L., & Coil, A. L. 2010, ApJS, 191, 43
Smith, B. D., Hallman, E. J., Shull, J. M., & O'Shea, B. W. 2011, ApJ, 731, 6
Sokasian, A., Abel, T., Hernquist, L., & Springel, V. 2003, MNRAS, 344, 607
Songaila, A. 2004, AJ, 127, 2598
Spergel, D. N., Verde, L., Peiris, H. V., et al. 2003, ApJS, 148, 175
Stark, D. P., Ellis, R. S., Chiu, K., Ouchi, M., & Bunker, A. 2010, MNRAS, 408, 1628
Trac, H., & Cen, R. 2007, ApJ, 671, 1
Trac, H., Cen, R., & Loeb, A. 2008, ApJL, 689, L81
Trac, H. Y., & Gnedin, N. Y. 2011, ASL, 4, 228
Trenti, M., Smith, B. D., Hallman, E. J., Skillman, S. W., & Shull, J. M. 2010, ApJ, 711, 1198
Turk, M. J., Smith, B. D., Oishi, J. S., et al. 2011, ApJS, 192, 9
Valageas, P., & Silk, J. 1999, AAP, 347, 1
Warren, M. S., Abazajian, K., Holz, D. E., & Teodoro, L. 2006, ApJ, 646, 881
Willott, C. J., Delorme, P., Reylé, C., et al. 2010, AJ, 139, 906
Wise, J. H., & Abel, T. 2011, MNRAS, 414, 3458
Wise, J. H., & Cen, R. 2009, ApJ, 693, 984
Wise, J. H., Demchenko, V. G., Halicek, M. T., et al. 2014, arXiv:1403.6123
Wyithe, J. S. B., Hopkins, A. M., Kistler, M. D., Yüksel, H., & Beacom, J. F. 2010, MNRAS, 401, 2561
Yajima, H., Choi, J.-H., & Nagamine, K. 2011, MNRAS, 412, 411
Zahn, O., Lidz, A., McQuinn, M., et al. 2007, ApJ, 654, 12